A priori study of subgrid-scale features in turbulent Rayleigh-Bénard convection

F.Dabbagh,[1, a)] F.X.Trias,[1, b)] A.Gorobets,[1, 2, c)] and A.Oliva[1, d)]

[1)] *Heat and Mass Transfer Technological Centre, Technical University of Catalonia, ESEIAAT, c/Colom 11, 08222 Terrassa, Spain*

[2)] *Keldysh Institute of Applied Mathematics, 4A, Miusskaya Sq., Moscow 125047, Russia*

(Dated: 24 August 2017)

At the crossroad between flow topology analysis and turbulence modeling, *a priori* studies are a reliable tool to understand the underlying physics of the subgrid-scale (SGS) motions in turbulent flows. In this paper, properties of the SGS features in the framework of a large-eddy simulation are studied for a turbulent Rayleigh-Bénard convection (RBC). To do so, data from direct numerical simulation (DNS) of a turbulent air-filled RBC in a rectangular cavity of aspect ratio unity and π spanwise open-ended distance are used at two Rayleigh numbers $Ra \in \{10^8, 10^{10}\}$ [PoF, 28, 115105 (2016)]. Firstly, DNS at $Ra = 10^8$ is used to assess the performance of eddy-viscosity models such as QR, WALE and the recent S3PQR-models proposed by Trias *et al.*[PoF, 27, 065103 (2015)]. The outcomes imply that the eddy-viscosity modeling smoothes the coarse-grained viscous straining and retrieves fairly well the effect of the kinetic unfiltered scales in order to reproduce the coherent large scales. However, these models fail to approach the exact evolution of the SGS heat flux and are incapable to reproduce well the further dominant rotational enstrophy pertaining to the buoyant production. Afterwards, the key ingredients of eddy-viscosity, ν_t, and eddy-diffusivity, κ_t are calculated *a priori* and revealed positive prevalent values to maintain a turbulent wind essentially driven by the mean buoyant force at the sidewalls. The topological analysis suggests that the effective turbulent diffusion paradigm and the hypothesis of constant turbulent Prandtl number are only applicable in the large-scale strain-dominated areas in the bulk. It is shown that the bulk-dominated rotational structures of vortex-stretching (and its synchronous viscous dissipative structures) hold the highest positive values of ν_t, however the zones of backscatter energy and counter-gradient heat transport are related to the areas of compressed focal vorticity. More arguments have been attained through *a priori* investigation of the alignment trends imposed by existing parameterizations for the SGS heat flux, tested here inside RBC. It is shown that the parameterizations based linearly on the resolved thermal gradient are invalid in RBC. Alternatively, the tensor-diffusivity approach becomes a crucial choice of modeling the SGS heat flux, in particular, the tensorial diffusivity that includes the SGS stress tensor. This and other crucial scrutinies on a future modeling to the SGS heat flux in RBC are sought.

a)firas@cttc.upc.edu

b)xavi@cttc.upc.edu

c)andrey@cttc.upc.edu

d)oliva@cttc.upc.edu

I. INTRODUCTION

Buoyancy-driven flows have always been an important subject of scientific studies with numerous applications in environment and technology. A famous example thereof is the thermally driven flow developed in a fluid layer heated from below and cooled from above, *i.e.* Rayleigh-Bénard convection (RBC)[1] (see Figure 1). It approaches many circulations in nature and industry, such as governing flows in nuclear reactors, solar thermal power plants, electronic devices, and convection in the atmosphere, oceans and deep mantle. Most of these flows are ruled by turbulent regime purely sustained by buoyancy, the reason that imparts a significant complexity into the flow system. Mainly, the chief dynamics therein such as the vortical structures and thermal plumes are essentially associated with immanent unsteadiness, energy nonequilibriums, strong pressure fluctuations and hardly interacted different size scales of motions[2]. Following the self-sustained cycle of the plumes, they produce alternative nonequilibriums between the buoyant production and the viscous dissipation, which are mainly compensated by the pressure transport mechanisms[3]. As a consequence, predicting the complex coherent dynamics in a turbulent RBC derives formidable challenges, particularly within the scope of turbulence modeling.

Direct numerical simulation (DNS) has provided a fruitful knowledge about the problem in the fields of coherent dynamics and turbulence physics[4,5]. Apart from overcoming the uncertainties pertaining to the experimental studies, DNS has allowed to investigate and resolve many queries in RBC at relatively high Rayleigh (Ra) numbers[6,7]. However, the full resolution of every generated vortical filament in DNS requires increasing computational demands with Ra. Therefore, in the foreseeable future, the numerical simulations of hard turbulent RBC will have to resort to turbulence modeling. An approach which has gained a considerable attention in the recent years is the Large-eddy simulation (LES). Therein, only the large-scale energy containing flow is computed directly and the influence of the small scale motions, which is assumed as isotropic and universal, is modeled. The key feature of LES depends on how properly the unresolved subgrid-scale (SGS) of the Reynolds stress and heat flux terms evolved in the filtered governing equations, are approximated. Following the prominent assumption of eddy-viscosity, ν_t, modeling, Eidson[8] extended the well-known Smagorinsky model by including the buoyant production contribution in evaluating ν_t for RBC. His results showed a good consistency with experiments at low numbers

of Ra, however, for hard turbulent regimes, they start to be occasionally erroneous with non-real behavior[9]. Peng and Davidson[9], later modified the Eidson's formula to remedy this problem. They applied the dynamic procedure[10,11] to compute the model coefficients. Then, in Ref. 12, they employed the dynamic Smagorinsky model in evaluating ν_t with the dynamic approach for the turbulent Prandtl number, Pr_t, used to calculate the eddy-diffusivity, κ_t, (gradient diffusion assumption). The dynamic procedure provided results that agree fairly well with DNS, however, this approach has multiple limitations. Namely, the averaging procedure in the periodic-directions is necessary in order to prevent numerical instabilities. This makes the dynamic approach less amenable for geometrically complex flows. Other authors as Czarnota *et al.*[13] had performed a comparative study using the dynamic Smagorinsky model and the dynamic scale similarity model for the momentum equation in RBC. They used the model of Peng and Davidson[14] for the SGS heat flux and showed that the dynamic Smagorinsky model produces occasionally unphysical temperature values. More recently, Foroozani *et al.*[15] have applied the Lagrangian dynamic technique[16] in the Smagorinsky model. The above-mentioned clipping of the dynamic procedure is overcome in the Lagrangian averaging, however, the procedure entails significant complexity and computational cost. In a general perspective, most of the aforesaid strategies of thermal turbulence modeling (LES) are restrained by such complexities, considerable cost and the necessity to use a dynamic technique in order to precisely follow the interacted scales of buoyant/strain production. Hence, a critical understanding of the problem dynamics in the frame of turbulence modeling performance is necessary.

Based on the DNS results, the statistical analysis of the SGS features becomes of great interest in verifying the assumptions of existing models. It can provide insights into the underlying physics of the small scale dynamics in the spirit of turbulence models. Hence, one can note how well the model matches the topological characteristics, *e.g.* the alignment trends, of the modeled quantities with respect to the resolved flow structures. In this work, we first investigate *a posteriori*, the performance of LES eddy-viscosity models, such as WALE, QR and the novel S3PQR[17] modeling, in RBC at $Ra = 10^8$. Therein, the SGS heat flux is modeled following the gradient transport hypothesis where the assumption of constant-Pr_t, is used. These models possess important properties, such as the simplicity and the ability to work in complex geometries without limitations. Afterwards, the key ingredients in the LES models of the eddy-viscosity ν_t, eddy-diffusivity κ_t and turbulent

Prandtl number Pr_t, are studied *a priori*. The analysis includes a statistical study of the underlying flow topology associated with the SGS components. Moreover, we investigate *a priori* the performance of SGS heat flux models defined in the frame of the gradient diffusion assumption (the SGS heat flux in aligned against the thermal gradient). Namely, we propose to judge the behavior of the most used SGS heat flux models such as Peng and Davidson[14] and Daly and Harlow[18] in the mixed model space, similar to Higgins *et al.*[19]. The data set used is based on our DNS results of an air turbulent RBC at $Ra = 10^8$ and 10^{10}, published in Dabbagh *et al.*[5].

The remainder of the paper is organized as follows. A short description of the DNS details in the current configurations of RBC is given in Section II. Then, a comparative test regarding the performance of such well-known eddy-viscosity models in LES is presented in Section III. Afterwards, *a priori* study over the SGS components of the Pr_t is included in Section IV. The statistical analysis of the SGS heat flux models is addressed in Section V, and a new approach towards a future modeling of the SGS heat flux in RBC is proposed. Finally, relevant results are summarized and conclusions are given.

II. DNS DESCRIPTION

We restrict ourselves to a rectangular geometry of aspect ratio unity–squared cross section–($\Gamma = W/H$) and longitudinal spanwise open-ended distance $L/H = \pi$ (see sketch in Figure 1). The adequacy of the spanwise domain size was studied in Refs. 5 and 20, where it was found that a size of $L/H = \pi$, is sufficient. L, W and H correspond to the physical real dimensions of the cavity, identified as, the length, width and the height, respectively. The cavity is filled with a Newtonian fluid of constant thermophysical properties, as the kinematic viscosity ν and thermal diffusivity κ. The fluid is transparent to the radiation with density variations and compressibility effects neglected. The only exception is the density variation in the buoyancy forces where the so-called Oberbeck-Boussinesq (OB) approximation[21,22], is used. Following theses assumptions, and in case of negligible thermal radiation and energy dissipation due to viscosity, the governing equations of continuity, Navier-Stokes (NS), and thermal energy, are given in non-dimensional form as,

$$\partial_t \boldsymbol{u} + (\boldsymbol{u}\cdot\nabla)\boldsymbol{u} = -\nabla p + (Pr/Ra)^{1/2}\nabla^2\boldsymbol{u} + \boldsymbol{f}, \qquad \nabla\cdot\boldsymbol{u} = \boldsymbol{0}, \tag{1}$$

$$\partial_t T + (\boldsymbol{u}\cdot\nabla)T = (RaPr)^{-1/2}\nabla^2 T, \tag{2}$$

where $\boldsymbol{u} = (u, v, w)$ is the velocity vector in Cartesian coordinates $\boldsymbol{x} = (x, y, z)$, p is the pressure field, $\boldsymbol{f} = (0, T, 0)$ is the body force vector and T is the temperature. These equations formulate the mathematical model that describes the flow dynamics in RBC. All quantities therein (in Eqs. 1 and 2) are made dimensionless by using the height of the fluid layer H, the temperature difference between the upper and the lower surfaces, $\Delta\Theta$, and the free-fall velocity, $U_{ref} = (\alpha g \Delta\Theta H)^{1/2}$. Meaning that U_{ref}, ρU_{ref}^2, $\Delta\Theta$ and H/U_{ref} are used as the characteristic scales for $\boldsymbol{u}$, p, T and time t, respectively, where α is the volumetric thermal expansion coefficient, g stands for the gravitational acceleration and ρ is the fluid density. The cavity is subjected to horizontal bottom and top constant dimensionless temperatures, $T_{hot} = 0.5$ and $T_{cold} = -0.5$, respectively, while the vertical walls are thermally insulated ($\partial T/\partial z = 0$). No-slip boundary conditions for the fluid ($\boldsymbol{u} = \boldsymbol{0}$) are imposed at all the four solid walls, and periodic boundary conditions are applied for all quantities in the longitudinal x-direction. The characteristic parameters of the system are introduced within the numbers of Prandtl $Pr = \nu/\kappa = 0.7$ and Rayleigh, $Ra = g\alpha\Delta\Theta H^3/\nu\kappa$, $Ra \in \{10^8, 10^{10}\}$, and in responding to that physics, the turbulent heat transport is established and determined by the Nusselt number, Nu, that is given by

$$Nu = \sqrt{RaPr}\langle vT\rangle_A - \partial\langle T\rangle_A/\partial y, \tag{3}$$

where the angular brackets operator $\langle\cdot\rangle$ indicates the temporal average (likewise it denotes the ensemble average in the statistical analysis), and the subscript symbol A refers to the average over the (x-z) plane at position y.

Numerically, Eqs.1 and 2 are spatially discretised on a Cartesian staggered grid using a finite-volume fourth-order symmetry-preserving scheme[23]. Regarding the temporal discretisation, a second-order self-adapting explicit scheme is used[24]. Then, the pressure-velocity coupling is solved by means of a classical fractional step projection method[25]. The grids are constructed with a uniform grid spacing in the periodic x-direction, while the wall-normal points are distributed following a hyperbolic-tangent function with an equal number of nodes ($N_y = N_z$), given in y-direction (identical for z-direction) by

$$y_i = \frac{1}{2}\left(1 + \frac{\tanh\{\sigma_y(2(i-1)/N_y - 1)\}}{\tanh\sigma_y}\right), \qquad i = 1, \ldots, N_y + 1, \tag{4}$$

where σ_y is the concentration factor in the y-direction. For more details about the DNS

procedures the reader is referred to Dabbagh *et al.*[5], and for the numerical methods, algorithms and verification of the DNS code, to Trias *et al.*[26]. RBC is normally identified with predominant thermal and kinetic dissipative small scales which are distributed differentially in the near-walls and the bulk regions[27]. This has always been an important demand to resolve both areas well in order to properly characterize the flow dynamics. To do so, a refinement approach based on the Grötzbach estimate[28] for the Kolmogorov scales, which is given by

$$\eta_{Grö} \leq \frac{\pi \, \mathrm{Pr}^{1/2}}{((Nu-1)Ra)^{1/4}} \quad \text{for} \quad Pr \leq 1, \tag{5}$$

has been considered firstly for the low Ra number. By introducing Δy_{max} as the maximum grid spacing applied in the core where $\Delta y_{max} = \Delta z_{max} = \Delta x$, various refinement ratios of the Grötzbach criterion defined as $\Delta y_{max}/\eta_{Grö} \in [1.1 \rightarrow 0.7]$, have been tested[20]. Furthermore, an investigation has been performed in order to reduce the computational cost by maximizing the equidistant spacing in the periodic x-direction (instead of setting it to $\Delta x = \Delta y_{max}$), at the same Ra number. The numerical tests in this regard have led to a refinement ratio of $\Delta y_{max}/\eta_{Grö} = 0.9$, and a coarsening tolerance for the homogeneous cell spacing in the range $\Delta x/\Delta y_{max} \in [1.25 \rightarrow 1.5]$, without losing accuracy. These results have later been used to choose the proper estimated grid at $Ra = 10^{10}$ (see table I). On the other hand, the BLs are resolved with $N_{BL} = 9$ and 12 grid points for $Ra = 10^8$ and 10^{10}, respectively. This exceeds the resolution requirements proposed by Shishkina *et al.*[29] and given, for $Pr \approx 0.7$, by:

$$N_{th.BL} \approx 0.35 Ra^{0.15}, \qquad 10^6 \leq Ra \leq 10^{10}, \tag{6}$$

$$N_{v.BL} \approx 0.31 Ra^{0.15}, \qquad 10^6 \leq Ra \leq 10^{10}, \tag{7}$$

where $N_{th.BL}$ and $N_{v,BL}$ are the minimum required number of nodes within the thermal and viscous BLs, respectively.

A summary of the DNS parameters and the relevant Nu results are included in Table I. The data set used in the present study corresponds to the statistically steady state. In this case, after at least 500 non-dimensional time units $[TU]$, the temporal integrations are started and continue during a sufficiently converging long periods, $\zeta = 500[TU](Ra = 10^8)$ and $200[TU](Ra = 10^{10})$, respectively (see time series and cumulative average statistics for T and T_{rms} at two monitoring points in Figure 2). The consecutive snapshots are gathered over several large eddy turnover times, ζ_{st} (see Table I), to ensure that the results are well-converged and data is temporally uncorrelated. Note that the large-eddy turnover time is

encountered in this DNS to last about $\tau_{eddy} \sim 7[TU](Ra = 10^8)$ and $5[TU](Ra = 10^{10})$, with the definition as $\tau_{eddy} = H/\boldsymbol{u}_{rms}$, where $\boldsymbol{u}_{rms}$ the root mean square of the velocity in the bulk. Identically to Ref. 5, the bulk region used in this paper, is defined as $V_{bulk} = \{\boldsymbol{x} = (x, y, z)|0.2 \leq y \leq 0.8; 0.2 \leq z \leq 0.8\}$.

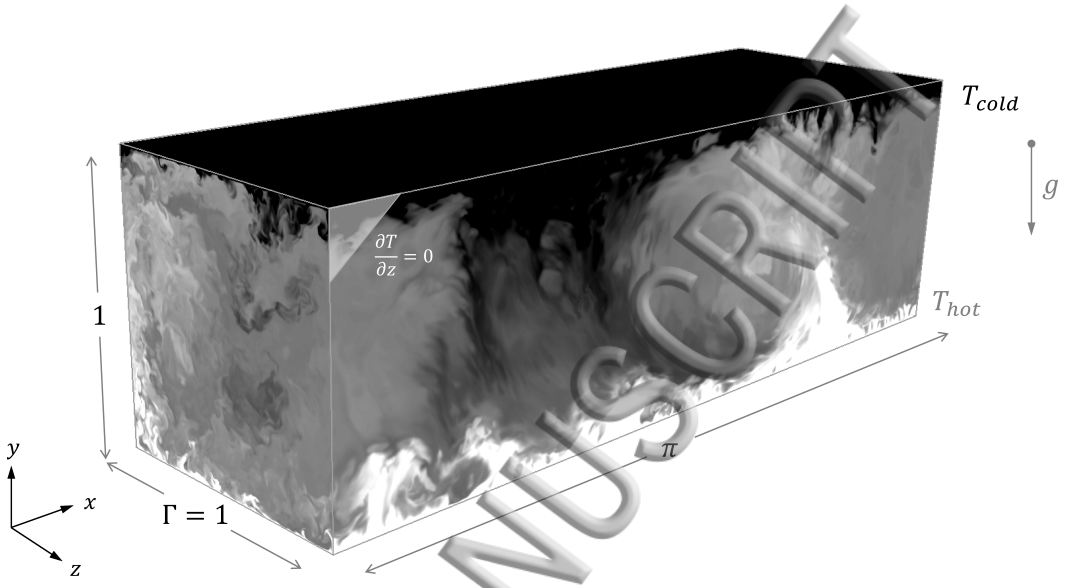

FIG. 1: Schema of the Rayleigh-Bénard configuration studied. Displayed together with a developed instantaneous temperature field taken of the DNS at $Ra = 10^{10}$.

III. LARGE-EDDY SIMULATION MODELS AND FLOW TOPOLOGY

The LES equations result from applying a spatial filtering to the governing equations (Eqs. 1 and 2), as following

$$\partial_t \bar{\boldsymbol{u}} + (\bar{\boldsymbol{u}} \cdot \nabla)\bar{\boldsymbol{u}} = -\nabla \bar{p} + (Pr/Ra)^{1/2}\nabla^2 \bar{\boldsymbol{u}} + \bar{\boldsymbol{f}} - \nabla \cdot \bar{\tau}, \qquad \nabla \cdot \bar{\boldsymbol{u}} = \boldsymbol{0}, \tag{8}$$

$$\partial_t \bar{T} + (\bar{\boldsymbol{u}} \cdot \nabla)\bar{T} = (RaPr)^{-1/2}\nabla^2 \bar{T} - \nabla \cdot \bar{\boldsymbol{q}}, \tag{9}$$

where $\bar{\boldsymbol{u}}$, $\bar{T}$ and $\bar{p}$ are respectively the filtered velocity, temperature and pressure. The filtered large scales above a filter length Δ in the Kolmogorov equilibrium, and which are more energetic and boundary conditions dependent, are resolved directly. However, the SGS turbulence that is assumed to be more isotropic in nature is modeled. Hereafter, the overbar-terminology $\bar{(\cdot)}$ refers to the filtered fields, while the non-overlined terms refer to DNS fields. The SGS stress tensor $\bar{\tau}$ and the SGS heat flux vector $\bar{\boldsymbol{q}}$, approximate the effect

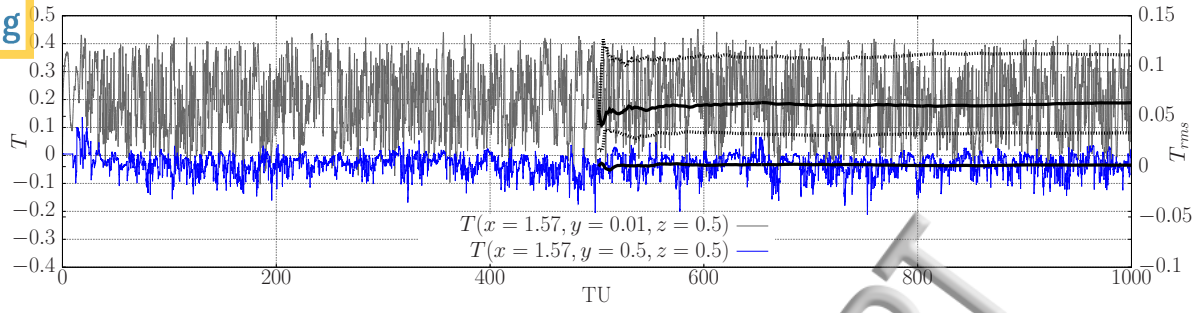

(a)

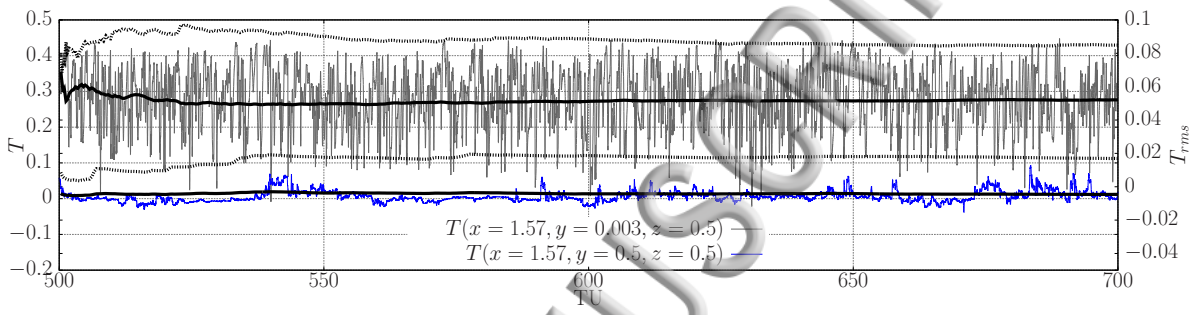

(b)

FIG. 2: Time series and cumulative average statistics (bold black lines) for T (solid) and T_{rms} (dashed), at two monitoring points, *i.e.* in the bulk and near isothermal hot plate for (a) $Ra = 10^8$ and (b) $Ra = 10^{10}$.

of the (small) under-resolved scales,

$$\bar{\tau} \simeq \overline{\boldsymbol{u} \otimes \boldsymbol{u}} - \bar{\boldsymbol{u}} \otimes \bar{\boldsymbol{u}}, \tag{10}$$

$$\bar{\boldsymbol{q}} \simeq \overline{\boldsymbol{u}T} - \bar{\boldsymbol{u}}\bar{T}, \tag{11}$$

and they need to be modeled in order to close the system. The most popular approach is the eddy-viscosity assumption, where the SGS stress tensor is computed in alignment with the local strain rate tensor, $\bar{\mathsf{S}} = 1/2(\nabla\bar{\boldsymbol{u}} + \nabla\bar{\boldsymbol{u}}^t)$, *i.e.*,

$$\bar{\tau} \approx -2\nu_t\bar{\mathsf{S}}. \tag{12}$$

In analogy to $\bar{\tau}$, the SGS heat flux is approximated employing the gradient-diffusion hypothesis, given as

$$\bar{\boldsymbol{q}} \approx -\kappa_t\nabla\bar{T}, \tag{13}$$

and the Reynolds analogy assumption is applied in evaluating κ_t. Namely, in a turbulent system the heat flux is assumed to be analogous to the momentum flux and its ratio therefore, is constant. In this case, the eddy-diffusivity, κ_t, is derived from the eddy-viscosity, ν_t, by

TABLE I: Summary of detailed parameters relevant to the DNS[5] and LES, providing the overall Nu results. η_{DNS} and η_{LES} are identically defined as $(\Delta x \Delta y \Delta z)^{1/3}_{max}$, N_{BL} refers to the imposed number of nodes inside the thermal boundary layers, Δt is the time step, and $\sigma_y = \sigma_z$ denotes to the concentration factor of grid points distribution in the corresponding direction. ζ indicates the averaging period used to compute the average flow and the turbulent statistics, whereas ζ_{st} is the number of large eddy turnover time during which consecutive snapshots are gathered to compute the statistical analysis.

DNS			LES ($Pr_t = 0.4$)		
	$Ra = 10^8$	$Ra = 10^{10}$	$Ra = 10^8$		
	$N_x \times N_y \times N_z$	$N_x \times N_y \times N_z$		Mesh A	Mesh B
Mesh	$400 \times 208 \times 208$	$1024 \times 768 \times 768$		$N_x \times N_y \times N_z$	$N_x \times N_y \times N_z$
				$120 \times 80 \times 80$	$168 \times 110 \times 110$
$\sigma_y = \sigma_z$	1.4	1.6	$\sigma_y = \sigma_z$	2	2
$\Delta t[TU]$	1.45×10^{-3}	4.14×10^{-4}	$\Delta t[TU]$	2.56×10^{-3}	1.46×10^{-3}
$\zeta[TU]$	500	200	$\zeta[TU]$	500	500
$\eta_{Grö}$	1.09×10^{-2}	2.46×10^{-3}	$\Delta x = (\Delta y = \Delta z)_{max}$	2.62×10^{-2}	1.87×10^{-2}
$\Delta y_{max}/\eta_{Grö}$	0.7	0.92	$(\Delta y = \Delta z)_{min}$	9.62×10^{-4}	6.90×10^{-4}
$\Delta x/\Delta y_{max}$	1.0	1.36	η_{LES}	2.62×10^{-2}	1.87×10^{-2}
			N_{BL}	6	8
$(\Delta y = \Delta z)_{min}$	8.31×10^{-4}	1.71×10^{-4}	Nu		
η_{DNS}	7.7×10^{-3}	2.50×10^{-3}	No-model	39.2	35.6
N_{BL}	9	12	S3QR	38.0	35.0
$\zeta_{st}[\tau_{eddy}]$	40	10	QR	38.6	35.4
			WALE	35.6	33.3
Nu	30.9	128.1	$\zeta_{st}^{\text{No-model}}[\tau_{eddy}]$	-	94
			$\zeta_{st}^{\text{S3QR}}[\tau_{eddy}]$	–	94

a constant turbulent Prandtl number Pr_t independent of the instantaneous flow conditions, as follows

$$\kappa_t = \nu_t / Pr_t. \tag{14}$$

An investigation of the underlying physics of the Pr_t and its determined constant value is presented in the next Section IV. In this section, the value of Pr_t is assigned to the most used value in literature[8], *i.e.* $Pr_t = 0.4$. The ν_t value is evaluated here within a comparative examination of three eddy-viscosity models such as QR, WALE and the novel S3PQR models[17] proposed by the authors. They all possess a list of desirable properties based on physical, numerical and practical arguments. For example, positiveness and locality (all three models), the proper cubic near-wall behavior (WALE and S3PQR), automatically switching off ($\nu_t = 0$) for 2D flows (S3PQR and QR), they are well-conditioned and do not

have any intrinsic limitation for statistically inhomogeneous flows (all). On the base of a combination of invariants of the resolved velocity gradient tensor $\bar{\mathsf{G}} \equiv \nabla\bar{\boldsymbol{u}}$, the foregoing models can be described in a unified framework[17]. Namely,

$$\nu_t^{S3QR} = (C_{s3qr}\Delta)^2 Q_{\bar{\mathsf{G}}\bar{\mathsf{G}}^t}^{-1} R_{\bar{\mathsf{G}}\bar{\mathsf{G}}^t}^{5/6}, \tag{15}$$

$$\nu_t^{QR} = (C_{qr}\Delta)^2 \frac{|R_{\bar{\mathsf{S}}}|}{-Q_{\bar{\mathsf{S}}}}, \tag{16}$$

$$\nu_t^{WALE} = (C_W\Delta)^2 \frac{(\mathsf{V}_{\bar{\mathsf{G}}}^2/2 + 2Q_{\bar{\mathsf{G}}}^2/3)^{3/2}}{(-2Q_{\bar{\mathsf{S}}})^{5/2} + (\mathsf{V}_{\bar{\mathsf{G}}}^2/2 + 2Q_{\bar{\mathsf{G}}}^2/3)^{5/4}}, \tag{17}$$

where $Q_{\bar{\mathsf{G}}\bar{\mathsf{G}}^t} = \mathsf{V}_{\bar{\mathsf{G}}}^2 + Q_{\bar{\mathsf{G}}}^2$ and $R_{\bar{\mathsf{G}}\bar{\mathsf{G}}^t} = -R_{\bar{\mathsf{G}}}^2$, are the second and the third invariants of the $\bar{\mathsf{G}}\bar{\mathsf{G}}^t$ tensor, respectively. $C_{(.)}$ is the model's constant determined as $C_{s3qr} = 0.762$[17], $C_W = \sqrt{0.5}$[30] and $C_{qr} = 1/\pi\sqrt{3/2}$[31], and $\mathsf{V}_{\bar{\mathsf{G}}}^2$ is the L^2-norm of the vortex-stretching vector $\mathsf{V}_{\bar{\mathsf{G}}}^2 = |\bar{\boldsymbol{\omega}}\bar{\mathsf{S}}|^2$. In a unified terminology, $\mathsf{S} = 1/2(\mathsf{G} + \mathsf{G}^t)$ and $\Omega = 1/2(\mathsf{G} - \mathsf{G}^t)$ are the rate-of-strain and rate-of-rotation tensors, respectively, where $\mathsf{G} \equiv \nabla\boldsymbol{u}$. Their invariants have an important physical meaning in identifying coherent structures[32–34]. For instance, the invariant $Q_\Omega = -1/2tr(\Omega) = 1/4|\boldsymbol{\omega}|^2$ is proportional to the enstrophy density and indicates the concentrated tube-like structures of high vorticity $\boldsymbol{\omega} = \nabla \times \boldsymbol{u}$; while the invariant $Q_\mathsf{S} = -1/2tr(\mathsf{S}^2)$ is proportional to the local rate of the viscous dissipation, $\epsilon = 2\nu\mathsf{S}\colon\mathsf{S}$. They are combined together to formulate the invariant $Q_\mathsf{G} = Q_\mathsf{S} + Q_\Omega$, as a criterion that determines the areas related to the enstrophy prevalence ($Q_\mathsf{G} > 0$), and the dominant viscous dissipation regions ($Q_\mathsf{G} < 0$). On the other hand, the third invariant $R_\mathsf{S} = -1/3tr(\mathsf{S}^3)$, contributes to the straining production term and stands with the enstrophy production to compose the third invariant, $R_\mathsf{G} = R_\mathsf{S} - tr(\Omega^2\mathsf{S})$. Its sign implies a structural geometrical categorization to tube-like ($R_\mathsf{G} < 0$) and sheet-like ($R_\mathsf{G} > 0$) flow patterns[35]. As a consequence, critical point topologies are classified in the $(Q_\mathsf{G}, R_\mathsf{G})$ space, following Chong *et al.*[32] to four main classes named as, stable focus/stretching, unstable focus/compressing, stable node/saddle/saddle and unstable node/saddle/saddle structures (see Figure 1 in Ref. 34).

A. *A posteriori* LES results

For the sake of low computational cost, we restrict our *a posteriori* analysis to the lowest turbulent case ($Ra = 10^8$). We use two coarse meshes for LES (Mesh A and Mesh B presented in Table I). The meshes are constructed keeping the same grid points distribution

This manuscript was accepted by Phys. Fluids. Click here to see the version of record.

ing for the DNS but with a coarser spatial resolution. The concentration parameters used $\sigma_z = \sigma_y$, have been modified in order to increase the boundary layer grid resolution. Regarding the numerical discretisation and algorithms used, all are adopted similarly to the DNS (Section II), where the same trusty converging periods (ζ) are employed. In this regard, it is worth mentioning that the symmetry-preserving spatial discretisation[23] forms an excellent starting point for LES. Namely, for coarse grids, the convective operator transports energy from resolved scales of motion to other resolved scales without dissipating any energy, as it should do from a physical point-of-view. This forms a very solid basis for testing the SGS models[36]. Concerning the spatial discretisation of the eddy-viscosity models, the approach proposed by Trias *et al.*[37] has been used. Table I shows detailed parameters relevant to LES, along with the DNS parameters, where the overall Nu results given by each model are presented. The performance of the eddy-viscosity models is assessed by a comparison with the DNS profiles of turbulent statistics such as, the turbulent kinetic energy and heat flux, averaged in time and homogeneous direction. The profiles are extracted at the midwidth plane ($z = 0.5$) and represented in Figures 3 and 4, respectively, for $\langle \bar{k} \rangle$ and $\langle \bar{v}' \bar{T}' \rangle$, on the two grids used, *i.e.* Mesh A (left) and Mesh B (right). The fluctuating quantities of the resolved fields are denoted here as $\bar{\phi}' = \bar{\phi} - \langle \bar{\phi} \rangle$. As it can be seen in Figure 3, the turbulent kinetics are fairly well predicted with the S3QR and WALE models, both in the bulk and the near-wall areas. They give an enhanced capturing of the kinetics evolution in comparison with the case of not using any model (the No-model case) at the coarser grid (Mesh A in Figure 3a). When the grid spacing becomes refined (in Mesh B), the turbulent energy contained in the unfiltered scales (SGS) is less. Hence, a subsequent grid refinement should asymptotically drive an LES to DNS and Mesh B is appropriately resolving the turbulent kinetic quantities in Figure 3b. Regarding the turbulent heat flux, all the models fail in predicting the fluctuated thermals, particularly in the near-wall areas. They seem to overestimate the turbulent heat flux peak, as shown in Figure 4, which is essentially related to the role of the thermal plumes in the bulk region (transitional area). As a result, the obtained Nu values are overestimated (see Table I) in all the models. Similar to Figure 3b, the modeling of turbulent heat flux performs better on the refined grid (Mesh B in Figure 4b). The effect of the SGS modeling on the coarser grid (Mesh A in Figure 4a) is more notable than on the refined grid (Mesh B), if we compare it with the No-model case (particularly in the bulk). Moreover, the more refined grid, the closer behavior between the LES modeling

This manuscript was accepted by Phys. Fluids. Click here to see the version of record.

and the No-model, till approaching the DNS mesh. Hence, in the case of hard turbulent regime, *i.e.* at $Ra = 10^{10}$, the trustworthy LES grid size is found to be of an excessive level. The structures at that Ra, have revealed a self-amplification of the (turbulent background) viscous straining ($-Q_S$), and simultaneously of enstrophy (Q_Ω)[5]. As a result, both buoyant and strain productions take place on scaled-down motions and require very refined grids.

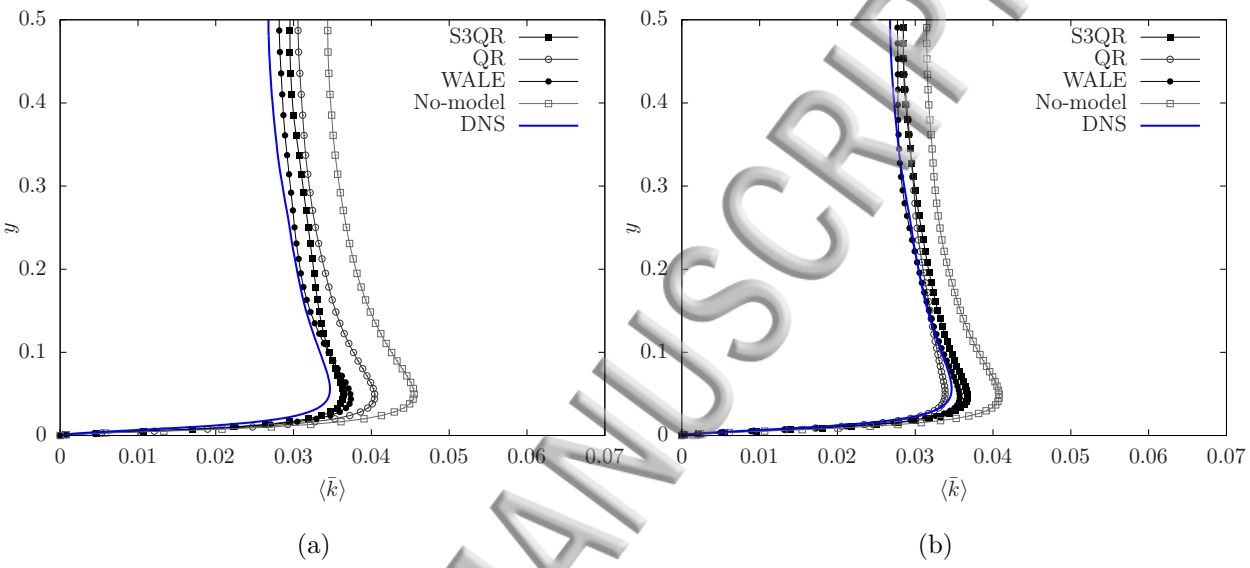

FIG. 3: Vertical profiles of the turbulent kinetic energy $\langle \bar{k} \rangle$, taken along the midwidth $z = 0.5$ plane and averaged in time and homogeneous x-direction on two grids, Mesh A (a) and Mesh B (b).

In order to explore the underlying influence of the SGS modeling, we conduct a statistical analysis related to flow topology classification and dominant small-scale physics for the cases of DNS, No-model and S3QR modeling. This last one is chosen as a representative LES modeling since no important differences among different models are observed. To do so, five joint probability density function (JPDF) spaces of invariant pairs pertaining to the velocity gradient tensor, normalized using $\langle Q_\Omega \rangle$ (following Ooi *et al.*[34]), have been considered in the bulk (V_{bulk}) at $Ra = 10^8$. The instantaneous data is gathered over adequate converging periods ($\zeta_{st}^{\text{No-model}}$ and ζ_{st}^{S3QR}, in Table I). Firstly, the JPDF of (Q_G, R_G) invariants plotted in Figures 5a,5b and 5c, reveals the well-known inclined "teardrop" shape as a universal feature of small-scale turbulence. Meaning that the fine flow patterns obey substantially stable tube-like vortex stretching structures and unstable sheet-like viscous dissipative structures in the bulk of RBC, as showed before in Ref. 5. It can be seen from Figure 5c that the S3QR model

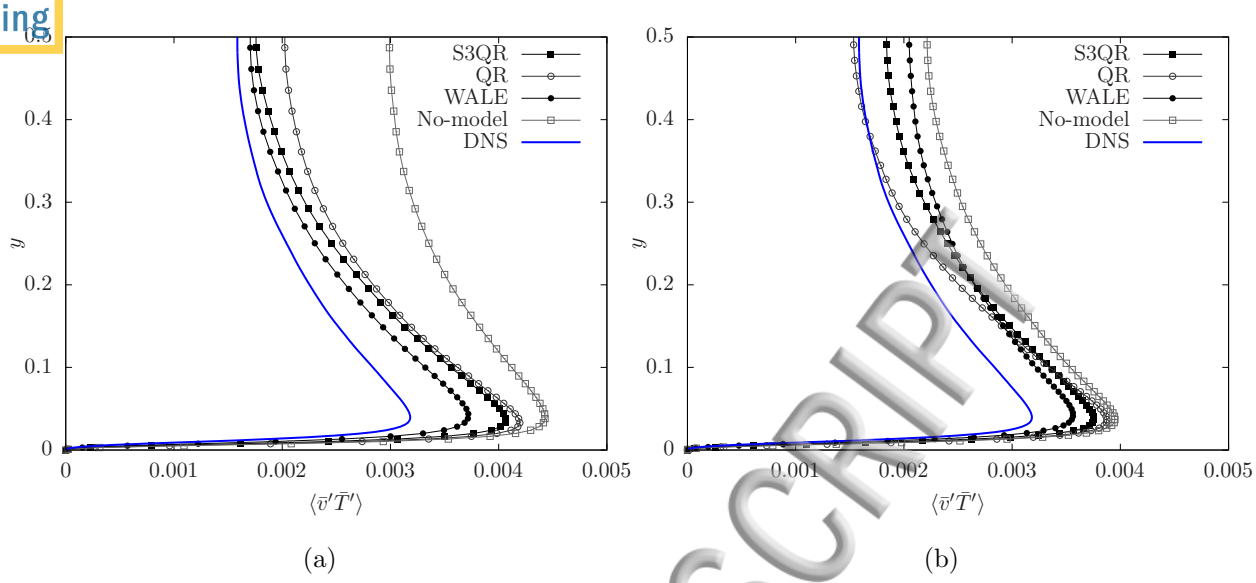

FIG. 4: Vertical profiles of the turbulent heat flux $\langle \bar{v}'\bar{T}' \rangle$, taken along the midwidth $z = 0.5$ plane and averaged in time and homogeneous x-direction on two grids, Mesh A (a) and Mesh B (b).

successfully reproduces the coherent large-scale structures placed normally near the origin. It retrieves the effect of the unfiltered scales at the filter length Δ and relaxes the spatial resolution in the dominant structures of tube-like vortex-stretching and sheet-like viscous dissipation. In contrast, Figure 5b displays highly dispersed distribution with excessive spatial viscous dissipation in the case of No-model. It reveals the coarse-grained velocity gradient distribution in the inertial range where the energy transfer is associated with the large negative straining ($R_S < 0$)[38]. In this span, it occurs on the axisymmetric contracted deformation aligned with the left null-discriminant tent-line ($D_G = 0$) in Figure 5b, or more evidently its counterpart $D_S = 0$ of (Q_S, R_S) space in Figure 5e. The (Q_S, R_S) map is particularly useful to analyze the geometry of the local straining of the fluid elements. As a universal aspect of turbulent flows, a strong preference for the zone $R_S > 0$, $Q_S < 0$, indicating a predominance of sheet-like structures to the kinetic energy dissipation, appears in Figures 5d,5e and 5f. It can be seen the well-smoothing of the small-scale effect retrieved to the large-scale shear by using the model in comparison with the case of the No-model, notably near the left $D_S = 0$ line. The $(-Q_S, Q_\Omega)$ map provides physical information about the dominant flow topologies with respect to the kinetic energy dissipation. The horizontal line Q_Ω represents points of high enstrophy but very small dissipation indicating the solid-body rotational at the center of the vortex tubes, while the vertical line $-Q_S$ represents

points of strong dissipation but little enstrophy density to indicate the irrotational straining outside and away from the vortex tubes. Balanced distribution of $Q_\Omega = -Q_S$ translates vortex sheet structures that normally occurs in the boundary layers. As showed in Ref. 5, the DNS in Figure 5g, manifests that the flow topology is mainly tube-like rotational in the bulk region, where the highest local value of $-Q_S$ is smaller than the highest local value of Q_Ω, and the JPDF is horizontally shifted towards the long-lived solid-body rotation. This grouping is reversed in the No-model case due to the high viscous dissipation produced, as shown in Figure 5h. However, the S3QR modeling displays a subtle balance between the rotational enstrophy and the strain dissipation in Figure 5i. It restrains the production of further enstrophy pertained to the buoyancy and thermal plumes in the bulk, and hence it is unable to capture well the subtle coupling of buoyant production and viscous straining. In fact, this can give a trend for the eddy-viscosity modeling to work better at very hard turbulent regime when the turbulent background dissipation is amplified enough (at much harder turbulence, $Ra > 10^{10}$). However, in this case, the modeling should keep in consideration two issues: the good prediction to the orientation of the SGS thermals and the high refined grid sufficient for the scaled-down straining. Finally, the invariants combination $(R_S - R_G/Q_\Omega, Q_\Omega)$ and $(R_S - R_G/Q_\Omega, -Q_S)$ spaces in Figure 6, indicate the underlying mechanisms of the vorticity magnitude to be amplified/reduced by the positive (stretched vortex)/negative (contracted vortex) sign of the stretching rate $(R_S - R_G)/Q_\Omega$, in relation to Q_Ω (enstrophy) and $-Q_S$ (strain rate) quantities. The DNS-based JPDF maps are displayed in Figures 6a and 6d, and show a persistent consistency with the isotropic turbulence behavior studied by Ooi *et al.*[34]. As shown in both Figures, most of the points in the flow have a positive stretching rate, and the enstrophy production is positive on average[5]. In Figure 6a, the high stretching rate is associated with regions of small Q_Ω implying that there is little evidence of self-stretching by strong enstrophy structures, as interpreted by Jiménez *et al.*[39]. On the contrary, Figure 6d shows a wider growing of stretching rate with increasing strain $-Q_S$ up to a certain value. In general, the magnitude of the stretching rate (stretching/compressing) is associated with regions of moderate to high $-Q_S$[34]. This in fact was also demonstrated in Dabbagh *et al.*[5], who emphasized on the local collaborating role of vortex compression $(R_S - R_G < 0)$ and strain generation $(R_S > 0)$, that always result in a positive contribution to the magnitude of the vortex-stretching vector. Regarding the S3QR modeling, it gives a refined and smoothed stretching rate alignment, reproducing the consistent DNS large-scale topology (Figures 6c

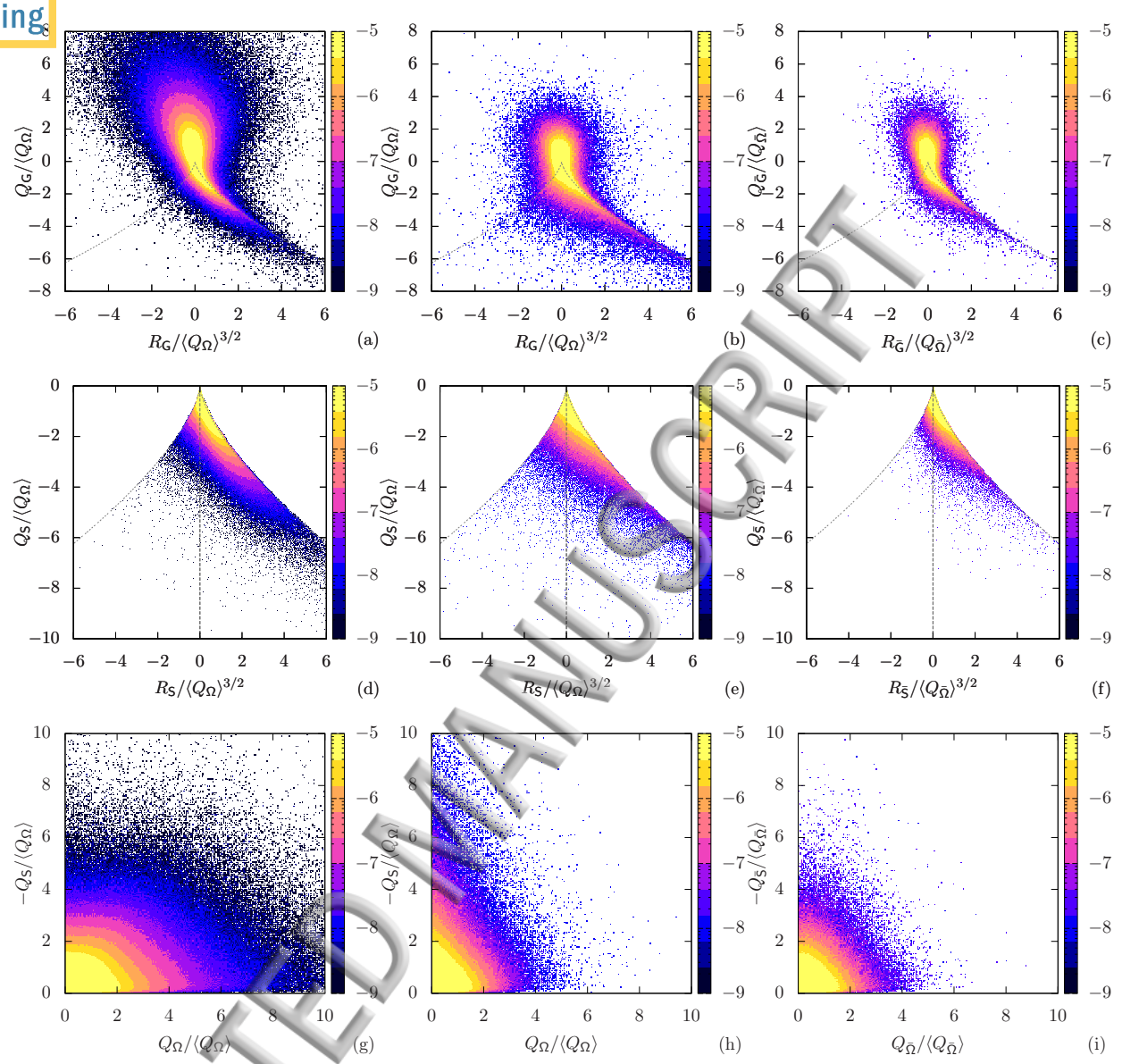

FIG. 5: JPDF of normalized invariants pair on logarithmic scale, for the corresponding DNS (left), No-model (middle) and S3QR-modeling (right). (Q_G, R_G) in (a,b,c), (Q_S, R_S) in (d,e,f), $(-Q_S, Q_\Omega)$ in (g,h,i). The data used are extracted from the bulk region at $Ra = 10^8$. Coarse-grained simulations (No-model and S3QR) correspond to Mesh B (see Table I). The dashed tent-lines therein refer to the corresponding null-discriminants.

and 6f). However, the No-model case produces coarse-grained higher magnitudes for all quantities, as displayed in Figures 6b and 6e.

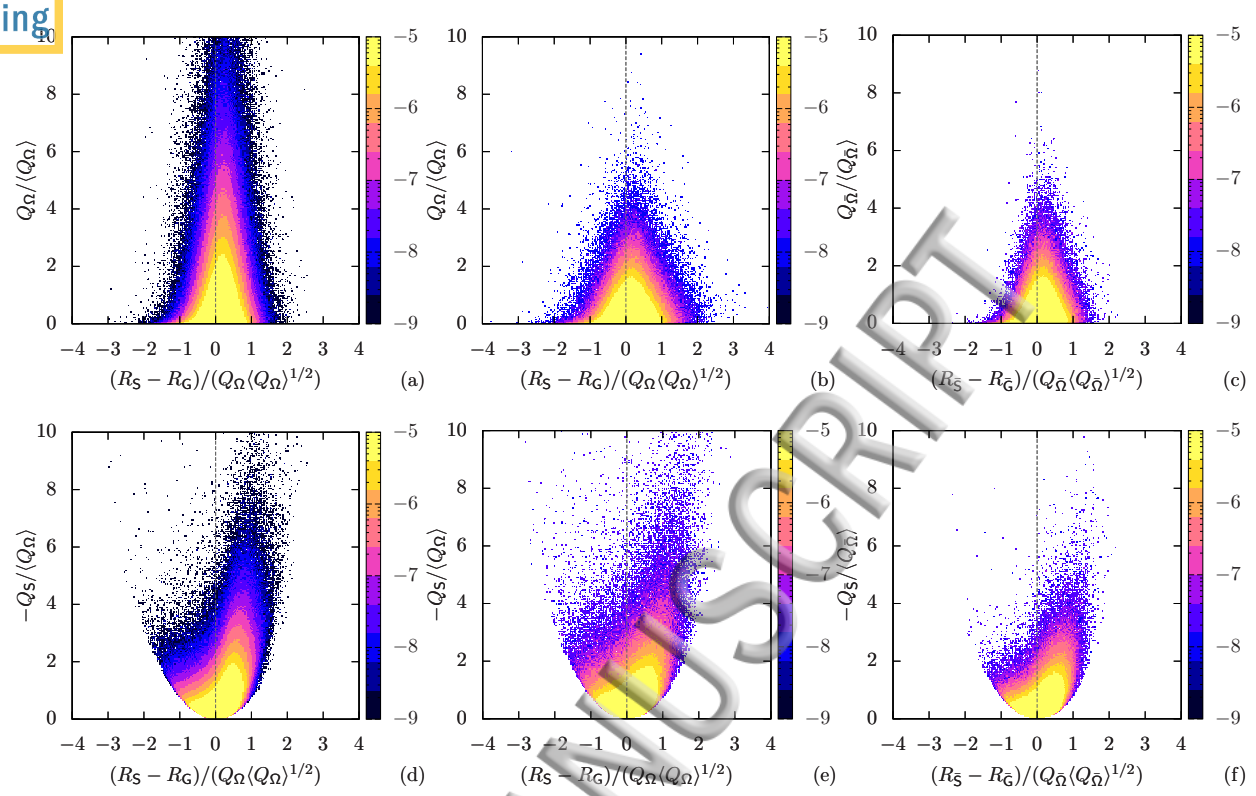

FIG. 6: JPDF of normalized invariants pair on logarithmic scale, for the corresponding DNS (left), No-model (middle) and S3QR-modeling (right). $(Q_\Omega, (R_S - R_G)/Q_\Omega)$ in (a,b,c), and $(-Q_S, (R_S - R_G)/Q_\Omega)$ in (d,e,f). The data used are extracted from the bulk region at $Ra = 10^8$. Coarse-grained simulations (No-model and S3QR) correspond to Mesh B (see Table I).

IV. TURBULENT PRANDTL NUMBER Pr_t

Turbulent Prandtl number is defined as the ratio between ν_t and κ_t, $(Pr_t = \nu_t/\kappa_t)$ indicating the balanced link between the subgrid-scale effects of thermals and kinetics in a turbulent system. It forms an extremely difficult quantity to measure in experiments, and intimately depends on the molecular fluid properties and the flow parameters[40]. For example, in the scope of the most used Reynolds analogy in considering a constant value of Pr_t, Kim and Moin[41] gave a range of the turbulent Prandtl number from 0.4 in the center to 1 near the walls of a forced convection heat transfer air channel flow. Pallares and Davidson[42] clarified that just a simple value $Pr_t = 0.4$ agrees well with the DNS and experiments. However, these results were restricted to an air flow ($Pr \sim 1$). In RBC, Eidson[8] also suggested a value of 0.4 in his model that included the SGS buoyant production

contribution in evaluating ν_t. In summary, different values can be found in the literature ranging from 0.1 to 1, according to Sagaut[43], in addition to the dynamic procedures (time and space dependent)[44] and temperature dependent[45] Pr_t models. The majority are sharing the behavior of flat profile of Pr_t in the bulk and increased maximum values near the wall in stratified and buoyancy-driven flows. In the present work, the Pr_t has been evaluated *a priori* using our DNS database. To do so, the right-hand-sides of Eqs. 10 and 11 have been approximated by the leading term of the Taylor series expansion, *i.e.* $\bar{\tau} \approx (\Delta^2/12)\mathsf{G}\mathsf{G}^t$ and $\bar{\boldsymbol{q}} \approx (\Delta^2/12)\mathsf{G}\nabla T$. Then, the values of ν_t and κ_t are obtained using a least square minimization in Eqs. 12 and 13, as follows

$$\nu_t \approx -(\Delta^2/12)\frac{\mathsf{G}\mathsf{G}^t : \mathsf{S}}{2\mathsf{S} : \mathsf{S}}, \qquad \kappa_t \approx -(\Delta^2/12)\frac{\mathsf{G}\nabla T \cdot \nabla T}{\nabla T \cdot \nabla T}. \tag{18}$$

This can result into a dynamical model of Pr_t, however with ill-conditioning properties. In this case, an ensemble temporal average procedure is necessary since it can produce negative diffusion (or eddy-viscosity), which potentially may lead to a blowup in the simulation[46,47]. Note that the leading terms of the Taylor series expansion of the SGS stress tensor and the SGS heat flux have been used. This result is the same for any convolution filter having a symmetric kernel[48], *e.g.* top-hat, Gaussian filters,... Furthermore, it is also worth mentioning that the value of filter length Δ is irrelevant in this analysis because it cancels out when computing the Pr_t and normalizing ν_t and κ_t. Plotting the averaged temporal-(x, z) profiles of these estimations, *i.e.*, $\langle\nu_t\rangle_A$, $\langle\kappa_t\rangle_A$ and $Pr_t = \langle\nu_t\rangle_A/\langle\kappa_t\rangle_A$ in Figure 7, various attributes can be observed. Mainly and in consistency with the literature, the turbulent Prandtl number reveals a similar behavior by taking a constant value through the bulk $Pr_t \approx 0.55$ that increases near the walls toward numbers larger than 1. Interestingly the value of Pr_t seems to be independent of Ra, and corresponds fairly well to the most popular literature value ($Pr_t = 0.4$). The profiles of the $\langle\nu_t\rangle_A$ and $\langle\kappa_t\rangle_A$ are positively skewed in average near the walls in agreement with the *a priori* analysis results of Kimmel *et al.*[49] and the dynamic models of Peng and Davidson[9]. Its distribution shape is relatively close to that one found in Peng and Davidson[9], taking into account the difference of the laterally confined domain and the higher turbulent regime considered here. Indeed, the findings of Burr *et al.*[50] also proposed the average positive prevalence of the turbulent energy production, *i.e.*, positive ν_t. They claimed in consequence, that the mean flow is driven by the mean buoyant forces and not by the Reynolds stresses associated with the turbulent

fluctuations (negative turbulent energy production and energy transport from fluctuations to the mean flow)[50]. A clearer picture can be attained from the averaged temporal-x plane of

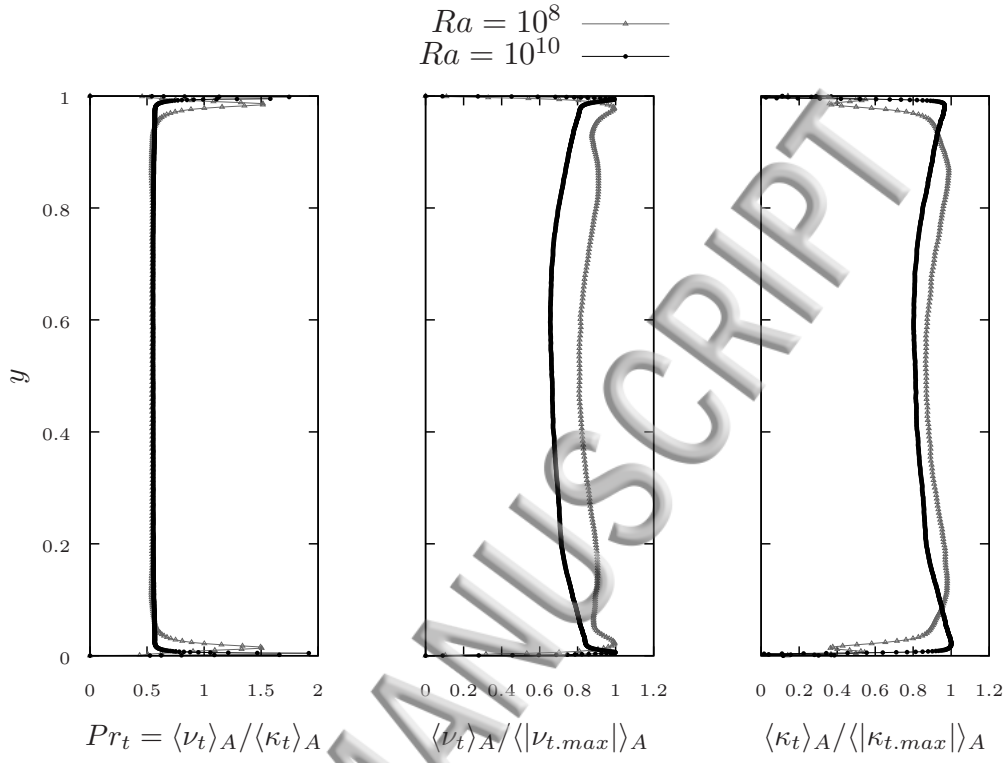

FIG. 7: Vertical profiles of the averaged time and (x, z) plane of ν_t and κ_t, evaluated from Eq. 18 and normalized by its maximals, and the consequent Pr_t.

$\langle\nu_t\rangle$ and $\langle\kappa_t\rangle$, shown in Figure 8 at $Ra = 10^8$ (the case that is clearer characterized by long-lived evolution of thermal plumes before getting shed in the bulk[5]). Therein, both terms reveal negative values limited in the corners of the lateral adiabatic sidewalls. Note that negative values of $\langle\kappa_t\rangle$ correspond to counter-gradient heat transport essentially generated by two mechanisms: one is due to the bulk dynamics and the other is due to the competition between the corner-flow rolls and the large-scale circulation[51]. The highest positive values of $\langle\kappa_t\rangle$ correspond to the tilted plumes traveling in groups within the vicinities of the sidewalls where the $\langle\nu_t\rangle$ values are very small (almost zero). While, next to the thermal BLs, $\langle\nu_t\rangle$ presents high positive magnitudes in regions of the impinging bulk dynamics (mixing action or the opposite-side plumes) to concentrate with four peaks of $\langle\nu_t\rangle$ in the four corners (see Figure 8, left). Such similar contours are observed in the case of $Ra = 10^{10}$ with much finer patterns of high negative and positive values in the near-wall vicinities. In conclusion, one can argue that the coherent mean mechanism in the current configurations obeys a

This manuscript was accepted by Phys. Fluids. Click here to see the version of record.

positive SGS eddy-viscosity and a turbulent wind driven by the mean buoyant forces at the sidewalls[50]. The buoyant sidewall-flow is mostly characterized by incorporating groups of swept rising-hot and falling-cold thermal plumes that were claimed to convey Reynolds stresses diverging[52]. These groups are eventually combined and produce buoyancy-driven upward/hot and downward/cold mean streams at one side and its opposite. This mean sidewall circulation becomes reduced significantly in the higher turbulent case at $Ra = 10^{10}$[5].

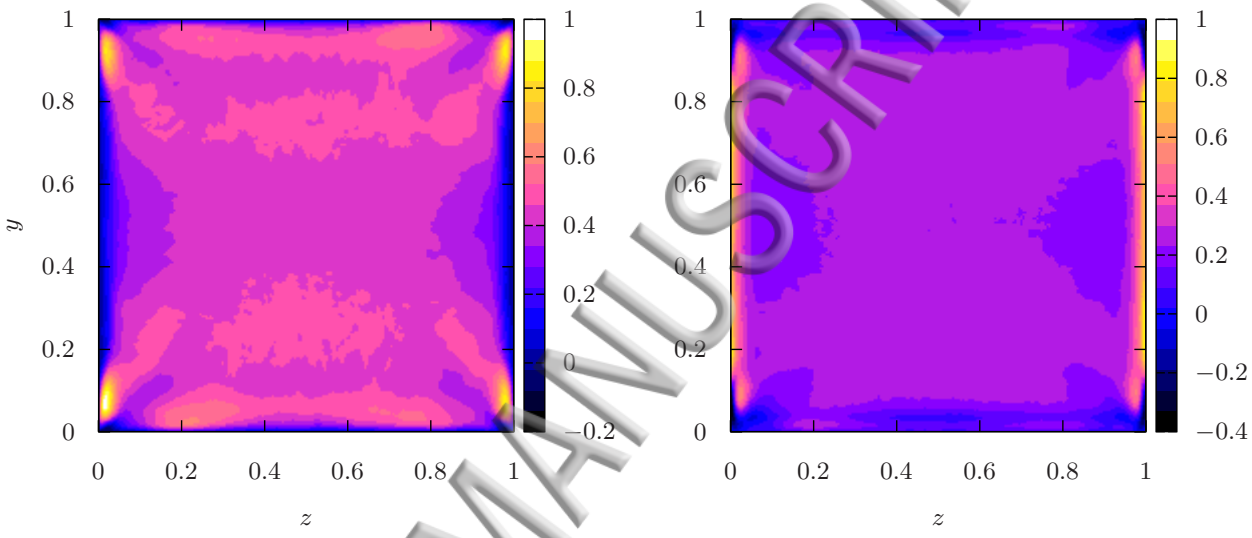

FIG. 8: Averaged time and homogeneous x-direction planes of ν_t (left) and κ_t (right), evaluated from Eq. 18 and normalized by its maximals.

In order to gain a quantitative understanding of the local underlying physics relevant to the SGS turbulence, the dominant flow topology associated with the positive and negative values of ν_t and κ_t, has been investigated. Similarly to many other turbulent flows[33–35] the small scale motions in turbulent RBC have manifested the inclined "teardrop" shape of the JPDF of invariants $(Q_{\mathsf{G}}, R_{\mathsf{G}})$, through the bulk[5](see Section III A). On condition of the "teardrop" distribution, the mean values of the eddy-viscosity and eddy-diffusivity are plotted in Figures 9a and 9b, through the bulk at $Ra = 10^8$. In other words, following the most probable JPDF of Q_{G} and R_{G} invariants, the average values of ν_t and κ_t, *i.e.*, $\langle \nu_t | (Q_{\mathsf{G}}, R_{\mathsf{G}}) \rangle$ and $\langle \kappa_t | (Q_{\mathsf{G}}, R_{\mathsf{G}}) \rangle$, are represented by a coloring in $(Q_{\mathsf{G}}, R_{\mathsf{G}})$ space. The plots are obtained on the base of sufficient statistical samples (> 150 per bin) in each pair of $(Q_{\mathsf{G}}, R_{\mathsf{G}})$ values. Furthermore, the invariants are normalized using $\langle Q_\Omega \rangle$ (following Ooi *et al.*[34]), and the SGS magnitudes are normalized by its maximum values (likewise Figures 7

and 8). From Figure 9b, it is evident that the highest positive values of κ_t hold unstable

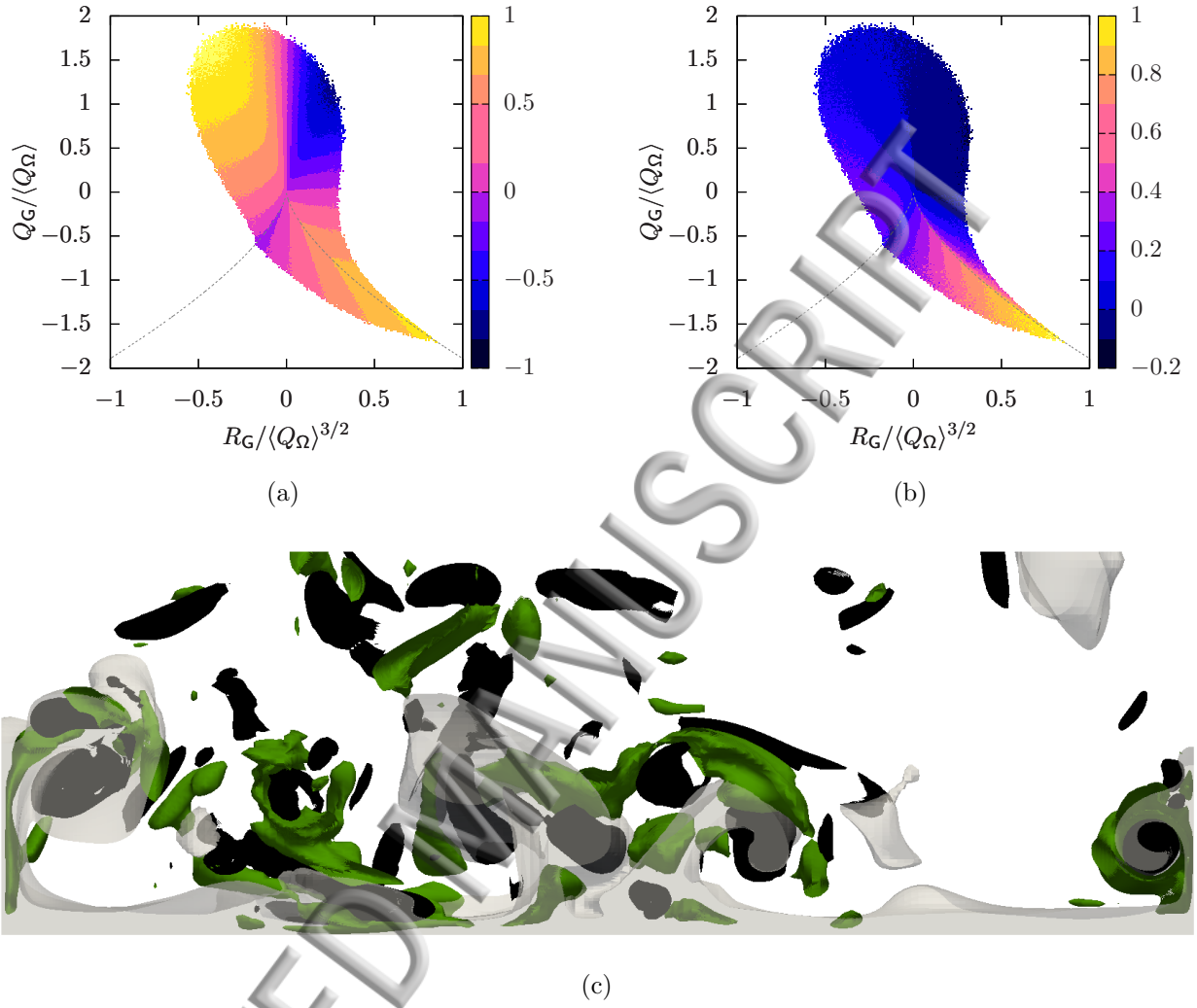

FIG. 9: $\langle \nu_t \rangle$ (a) and $\langle \kappa_t \rangle$ (b), conditioned on (Q_G, R_G) invariants space and normalized by its maximals. The results are obtained from the case of $Ra = 10^8$ through the bulk (V_{bulk}), and the dashed tent-lines refer to the null-discriminant $D_G = 0$ in (a) and (b). (c) Displays structures of sheet-like straining (colored green and identified by $Q_G < -14.29$ and $R_G > 0$) and tube-like vortex-stretching (colored black and identified by $Q_G > 14.29$ and $R_G < 0$), inside and outside the hot plumes (gray volumes). The section is taken from instantaneous fields at $Ra = 10^8$.

sheet-like strain-dominated areas ($Q_G < 0$ and $R_G > 0$). This exactly matches the observation of Chumakov[53], who performed *a priori* study of the SGS flux of a passive scalar in isotropic homogeneous turbulence. He claimed that *the effective turbulent diffusion paradigm is only applicable in the strain-dominated areas*, with more frequency around the right null-

discriminant line ($D_{\mathsf{G}} = 27/4R_{\mathsf{G}}^2 + Q_{\mathsf{G}}^3 = 0$). This explains the ability of the counter-gradient models (such as Eq. 13) to provide a feasible, but crude, average approximation to the SGS scalar flux for large LES cell sizes[53] (note the enhanced function of LES models on the coarser grid, *i.e.* Mesh A, in Section III A). The effective turbulent eddy-diffusivity occupy the viscous dissipative structures, which are presumed to be the mean sheet-like parts of the mushroom-like plumes elongated and scattered in the bulk (see Figure 9c). These sheets wrap around the tube-like vortex-stretching structures (Figure 9c) where the value of the turbulent diffusion κ_t is decreasing towards very small values in the stretching core (Figure 9b). Alternatively, the highest positive values of ν_t obey the structures of focal concentrated enstrophy ($Q_{\mathsf{G}} > 0, R_{\mathsf{G}} < 0$) and the synchronous strain-dominated areas ($Q_{\mathsf{G}} < 0, R_{\mathsf{G}} > 0$), as can be seen in Figure 9a. The turbulent viscosity appears to follow the small scale prevalent dynamics with positive value domination, in harmony with the fact that the flow topology is mainly tube-like rotational in the bulk region, as revealed in Section III A. Indeed, the association of negative eddy-viscosity regions with an increased anisotropy in RBC, was outlined before by Liberzon *et al.*[54]. This, in turn, supports our findings since the turbulence type in the core region of RBC is always comparable, in statistical aspects, with the isotropic nature[5]. Note that both SGS features maintain negative values in the areas of focal vortex contraction ($Q_{\mathsf{G}} > 0, R_{\mathsf{G}} > 0$), which play an important role in the turbulence amplification (non-linear advection) and the kinetic cascade energy mechanism. This proposes the sustainment of the backscatter kinetic energy[55] and the counter-gradient buoyancy flux in the areas of compressed vortex tubes through the bulk. Finally, both ν_t and κ_t are interestingly positive and hold an identical distribution in the large-scale strain-dominated regions. This may lead us to the theory that the constant turbulent Prandtl number hypothesis (linear assumptions) is only applicable in that area.

One can support this from the distribution of the turbulent Prandtl number conditioned on $(Q_{\mathsf{S}}, R_{\mathsf{S}})$ space, *i.e.*, $Pr_t = \langle \nu_t | (Q_{\mathsf{S}}, R_{\mathsf{S}}) \rangle / \langle \kappa_t | (Q_{\mathsf{S}}, R_{\mathsf{S}}) \rangle$, in Figure 10. The allocation of the most bulk-dominated value *i.e.*, $Pr_t = 0.55$, in the strain-dominated areas, can be observed. It concentrates close to the axisymmetric expansion (right tent-line of null-discriminant straining $D_{\mathsf{S}} = 27/4R_{\mathsf{S}}^2 + Q_{\mathsf{S}}^3 = 0$) where the local geometry of dissipation takes the sheet-like structures. Note also that $Pr_t = 0$ when $R_{\mathsf{S}} = 0$, at which the flow is mostly identified as two-dimensional.

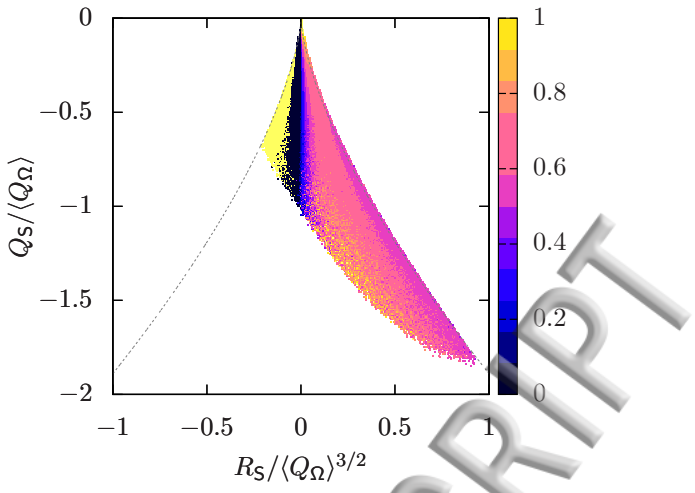

FIG. 10: $Pr_t = \langle \nu_t \rangle / \langle \kappa_t \rangle$ conditioned on (Q_S, R_S) invariants space. The results are obtained from the case of $Ra = 10^8$ through the bulk (V_{bulk}), and the dashed tent-line refer to the null-discriminant $D_S = 0$.

V. *A PRIORI* STUDY OF THE SGS HEAT FLUX MODELS

Most of the parameterizations used in LES of RBC are based on the assumption that the SGS heat flux is aligned against the spatial gradient of the resolved temperature (Eq. 13). Typically these parameterizations are tested by implementing them in model runs, and comparing the outcome of the simulations *a posteriori*, with the available data. The modeled results will be of integrated nature including a limited accuracy of the temporal and spatial numerical discretisation used. Hence, the assessment of models performance *a posteriori*, sometimes may not provide the needed insight into the physical robustness of the parameterizations. A more direct approach, *a priori* testing, can allow an excellent judgment on the validity of existing models. It can provide valuable data to test the behavior of the models and eventually can help to improve them. Such examples on testing the SGS scalar modelings can be found in studying the alignment trends of the SGS passive scalar in isotropic turbulence[53], and similarly in the atmospheric boundary layer[19]. In this context, we study the geometric alignment trends of the SGS heat flux vector $\bar{\boldsymbol{q}}$ derived from the Taylor series expansion[46] in comparison with $\bar{\boldsymbol{q}}$ parameterizations. This derivation is generic for a wide class of symmetric filters defined in real space such as the Gaussian, the top-hat and (almost) all the discrete filters[56]. The spatial derivatives make the SGS flux invariant under the change of sign of large-scale components, and which in turn allows the reversibility dynamics[56]. Generally, using the first two terms of the Taylor series expansion

This manuscript was accepted by Phys. Fluids. Click here to see the version of record.

ing a Gaussian filter[56], applied to our DNS database, we obtain an accurate prediction of $\bar{\boldsymbol{q}}$, as follows

$$\bar{\boldsymbol{q}} \approx \frac{\Delta^2}{12}\mathsf{G}\nabla T + \frac{\Delta^4}{288}\begin{pmatrix} \mathsf{H}(u)\colon \mathsf{H}(T) \\ \mathsf{H}(v)\colon \mathsf{H}(T) \\ \mathsf{H}(w)\colon \mathsf{H}(T) \end{pmatrix}, \qquad (\equiv \boldsymbol{q}) \tag{19}$$

where $\mathsf{H}(\phi) = \nabla\nabla\phi$ is the Hessian of a scalar field ϕ. Similarly, on the base of the down temperature gradient closure, the classical parameterizations for $\bar{\boldsymbol{q}}$ in LES, such as the Smagorinsky eddy-diffusivity model[57], can be approximated as

$$\bar{\boldsymbol{q}} \approx -\nu_t Pr_t^{-1}\nabla T = -(C_s\Delta)^2 Pr_t^{-1}|\mathsf{S}|\nabla T \qquad (\equiv \boldsymbol{q}^{eddy}), \tag{20}$$

where C_s is the model's constant, and the tensor diffusivity (or nonlinear) model[46], is approached (taking the first term of Eq. 19) as

$$\bar{\boldsymbol{q}} \approx \frac{\Delta^2}{12}\mathsf{G}\nabla T \qquad (\equiv \boldsymbol{q}^{nl}). \tag{21}$$

Both Eq. 20 and 21, are combined linearly in the so-called mixed model[19], as

$$\bar{\boldsymbol{q}} \approx \frac{\Delta^2}{12}(\mathsf{G}\nabla T - \Lambda|\mathsf{S}|\nabla T) \qquad (\equiv \boldsymbol{q}^{mix}), \tag{22}$$

where Λ is the ratio of corresponding model coefficients.

Similarly to the approach proposed by Higgins *et al.*[19], we construct the same space of the so-called "mixed model span"[19], defined as the plane containing the vectors ($\boldsymbol{q}^{eddy}$, $\boldsymbol{q}^{nl}$), and the normal to the mixed span $\boldsymbol{q}^{eddy} \times \boldsymbol{q}^{nl}$. A sketch of the geometry and definition of angles used is presented in Figure 11b. In this framework, we consider $\boldsymbol{q}$ (derived in Eq. 19) as the actual SGS heat flux, evaluated from the DNS database, and we study its alignments in that space. To do so, the JPDF of the angles α and β, defined together with γ, as

$$\alpha = \cos^{-1}\left[\frac{(\boldsymbol{q}^{eddy}\times\boldsymbol{q}^{nl})\cdot\boldsymbol{q}}{|\boldsymbol{q}^{eddy}\times\boldsymbol{q}^{nl}||\boldsymbol{q}|}\right], \quad \beta = \cos^{-1}\left[\frac{\boldsymbol{q}^{eddy}\cdot\boldsymbol{q}^{p}}{|\boldsymbol{q}^{eddy}||\boldsymbol{q}^{p}|}\right], \quad \gamma = \cos^{-1}\left[\frac{\boldsymbol{q}^{eddy}\cdot\boldsymbol{q}^{nl}}{|\boldsymbol{q}^{eddy}||\boldsymbol{q}^{nl}|}\right], \tag{23}$$

is plotted on the unit sphere. $\boldsymbol{q}^{p}$ is the projection of the heat flux onto the plane spanned by the mixed model, *i.e.* the portion of heat flux that can be expressed by the mixed model. This JPDF quantifies the relative frequency of orientations of the SGS heat flux vector in respect to the defined coordinates. In addition, a single probability density function (PDF) of γ is shown at the bottom of each plot to characterize the alignment of the tensor diffusivity vector $\boldsymbol{q}^{nl}$ with respect to the eddy-diffusion vector $\boldsymbol{q}^{eddy}$. The lower turbulent

regime at $Ra = 10^8$ within the bulk (V_{bulk}) has been considered since no significant changes are observed respecting $Ra = 10^{10}$. We firstly examine the influence of the characteristic length-scale, Δ, and the high-order spatial derivatives, *i.e.* the second term in Eq. 19, in Figure 11. Two different length-scale *i.e.* $\Delta = 2\eta_{DNS}$ and $8\eta_{DNS}$, are chosen where η_{DNS} is the maximum DNS grid size defined in Table I. One can clearly note the influence of Δ in reducing the effect of the Hessian multiplication (Figures 11a and 11c). From Figure 11d, the high-order derivatives tend to diffuse the direction of the SGS heat flux towards the normal to the span mixed model, but with a maintenance of maximal alignment within that span. This coincides to some extent with the findings of Higgins *et al.*[19] that reported the validity of the mixed-model span in describing the most likely orientations of the measured SGS heat flux in the lower atmosphere. Similarly here, the SGS heat flux points its nonlinear approach (Eq. 21) with shifted preferential orientations towards the equatorial plane defined as a linear combination of $\boldsymbol{q}^{nl}$ and $\boldsymbol{q}^{eddy}$ (Figure 11c). Note that the JPDF is symmetric about the equator and just the front part of the unit sphere which contains the peak of the PDF is shown. On the other hand, our results are also in perfect harmony with the alignment outcomes of the SGS passive scalar in isotropic homogeneous turbulence[53]. Therein, the SGS flux is approached following Eq. 21 in *a priori* analysis, and found to be misaligned with the vector of the resolved gradient (Eq. 20), similarly shown at the bottom of each plot in Figure 11. In conclusion, one can corroborate the failure of the isotropic eddy-diffusivity parameterization ($\boldsymbol{q}^{eddy}$) in turbulent RBC. It can be argued that the rotational geometries Q_Ω are prevalent in the bulk over the strain slots and $\Omega = \mathsf{G} - \mathsf{S}$ is an antisymmetric tensor that thus rotates the thermal gradient vector to be almost perpendicular to $\boldsymbol{q}^{nl}$ (note also that κ_t is almost zero in regions of focal concentrated enstrophy as shown in Section IV). Apart from that, the physical nature of the problem imposes a streamwise component of buoyant production as a SGS heat flux which is separated and should not be vanished by the (mean) large-scale thermal gradient components in the bulk[2].

In the same unified framework, we consider the constitutive relation of Daly and Harlow[18] based on the averaged Reynolds stresses in modeling the SGS heat flux within RANS (Reynolds-averaged Navier-Stokes) method, and which has been justified as a reasonable assumption for locally-averaged flows in Chumakov[53]. Namely, by employing the same approximation as in Section IV for the filtered-scale stress, *i.e.* $\bar{\tau} \approx (\Delta^2/12)\mathsf{G}\mathsf{G}^t$, Daly and

This manuscript was accepted by Phys. Fluids. Click here to see the version of record.

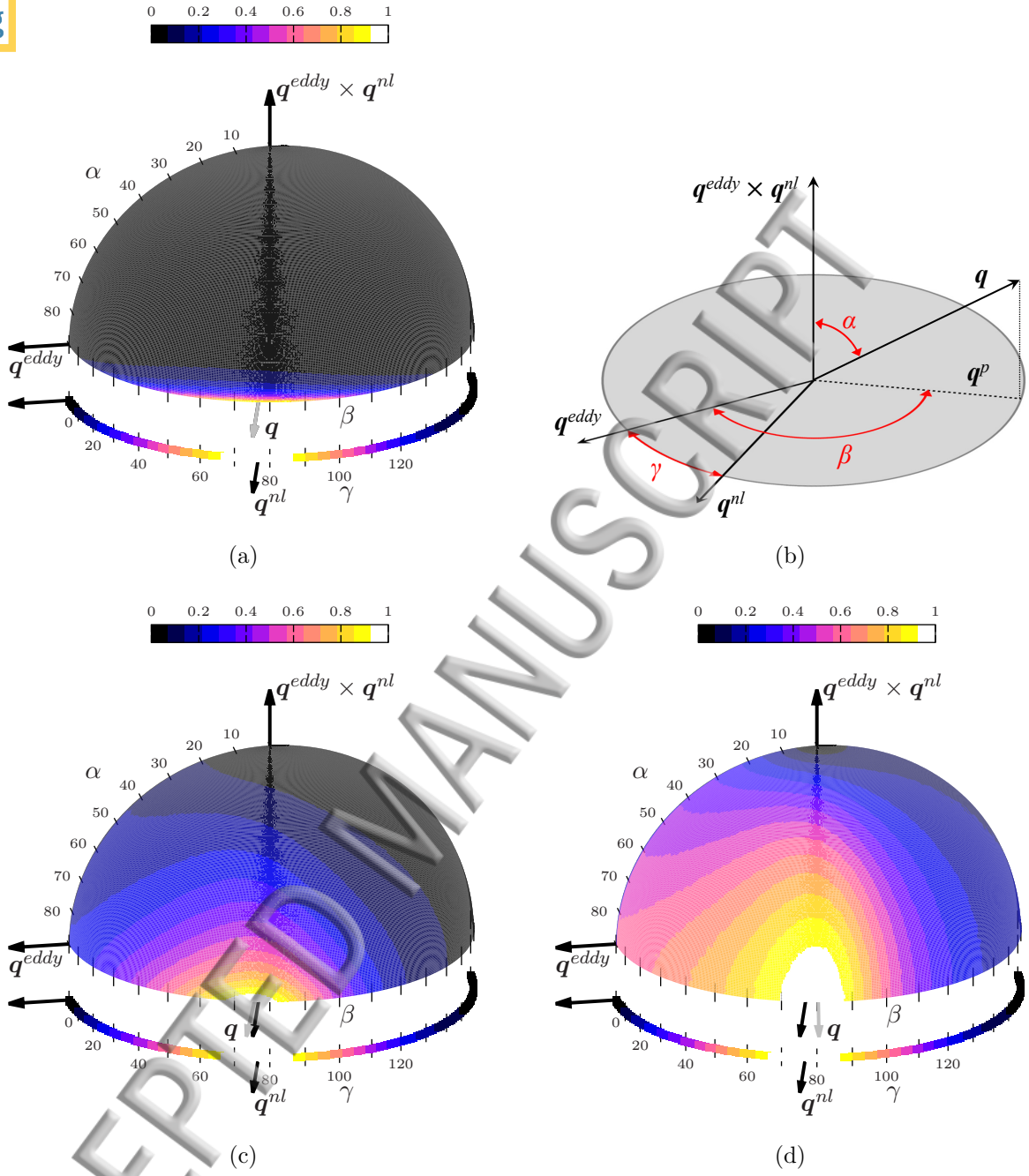

FIG. 11: JPDF of the angles (α, β) defined in Eqs. 23, and plotted on a half of unit sphere to exhibit the orientation trends of $\boldsymbol{q}$ in the space of the mixed model. (a) Shows the alignment trends when the length-scale $\Delta = 2\eta_{DNS}$, (c) represents the case of $\Delta = 8\eta_{DNS}$ and (d) displays the case of $\{\mathsf{H}(u)\colon \mathsf{H}(T), \mathsf{H}(v)\colon \mathsf{H}(T), \mathsf{H}(w)\colon \mathsf{H}(T)\}$. The PDF of γ is shown along the bottom strip of each chart. A sketch of definitions the angles used in the data analysis is presented in (b). For comparative and simplicity reasons the JPDF and PDF magnitude are normalized by its maximals.

Harlow model[18] is approached in *a priori* test, as

$$\bar{\boldsymbol{q}} \approx -\mathcal{T}_{SGS}\bar{\tau}\nabla T = -\frac{\Delta^2}{12}|\mathsf{S}|^{-1}\mathsf{G}\mathsf{G}^t\nabla T \qquad (\equiv \boldsymbol{q}^{DH}), \tag{24}$$

where $\mathcal{T}_{SGS} = 1/|\mathsf{S}|$ is an appropriate SGS timescale[53]. Moreover, the model proposed by Peng and Davidson[14] that also invokes a tensorial eddy-diffusivity as in Ref. 18. Instead, $\bar{\tau}$ is estimated by the eddy-viscosity model, *i.e.*, $\bar{\tau} \approx -2\nu_t\mathsf{S}$, and $\mathcal{T}_{SGS} \propto \Delta^2/\nu_t$, yielding to

$$\bar{\boldsymbol{q}} \approx C_t\Delta^2\mathsf{S}\nabla T \qquad (\equiv \boldsymbol{q}^{PD}), \tag{25}$$

where C_t is a model coefficient. The ability of the last two parameterizations is investigated in the same mixed model coordinates. Namely, we replace $\boldsymbol{q}$ in Figure 11 by its estimated vectors and observe the dominant orientations resulted by the models in relevant to the mixed model space. As shown in Figure 12, it seems that both parameterizations are preferentially

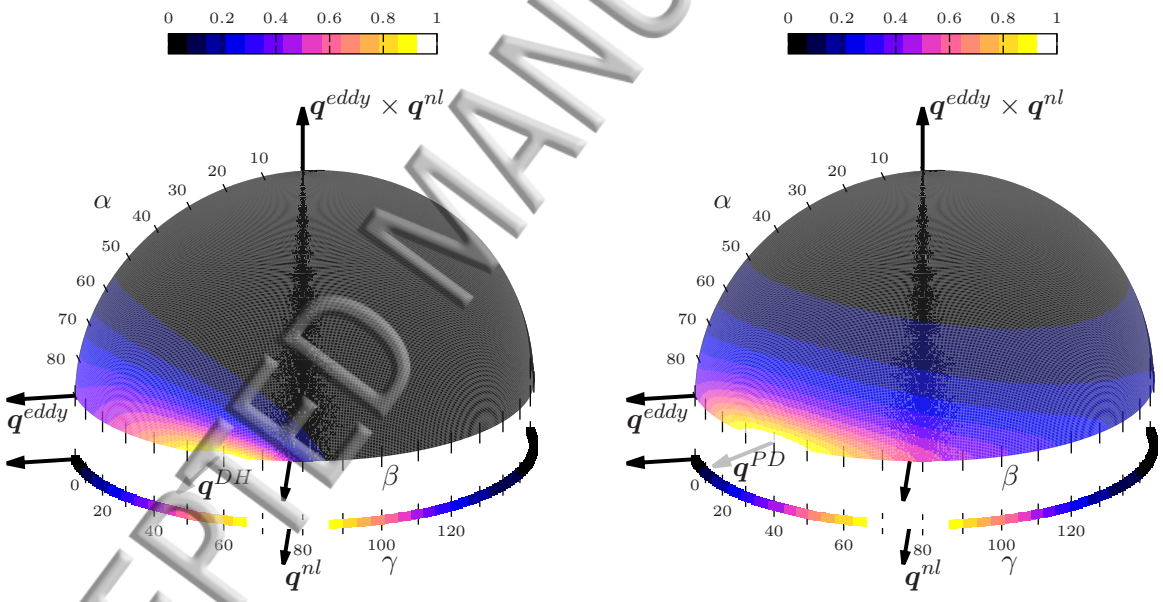

FIG. 12: The same JPDF charts represented in Figure 11, however, $\boldsymbol{q}$ is replaced by (a) Daly and Harlow relation[18] ($\boldsymbol{q}^{DH}$) and (b) Peng and Davidson model[14] ($\boldsymbol{q}^{PD}$).

pointing in the span of the mixed model, similar to the actual SGS heat flux $\boldsymbol{q}$. This confirms the fairly good validity of the mixed model in turbulent RBC. It is interesting to note that the assumption of Daly and Harlow ,$\boldsymbol{q}^{DH}$, gives a better prediction and closely approaches the direction of $\boldsymbol{q}^{nl}$. In contrast, the straining diffusivity assumption of Peng and

Davidson model, $\boldsymbol{q}^{PD}$, points towards the direction of the linear model, $\boldsymbol{q}^{eddy}$, and thus it can be worse/less applicable in RBC. This is not so strange and supports the collaborating sustainment of the streamwise SGS heat flux with the thermal gradient in the presence of dominant shear stress. In order to give a clear explanation, the alignment of the thermal gradient vector is studied in the space of rate-of-strain eigenframe, in Figure 13a. The three orthogonal eigendirections ($\boldsymbol{s}_1$, $\boldsymbol{s}_2$, $\boldsymbol{s}_3$) therein, represent the eigenvectors of S, in correspondence to the three eigenvalues ($\lambda_1^{\mathsf{S}}, \lambda_2^{\mathsf{S}}, \lambda_3^{\mathsf{S}}$). Since the velocity field is divergence-free, $\lambda_1^{\mathsf{S}} + \lambda_2^{\mathsf{S}} + \lambda_3^{\mathsf{S}} = 0$, and the eigensystem can be ordered $\lambda_1^{\mathsf{S}} \geqslant \lambda_2^{\mathsf{S}} \geqslant \lambda_3^{\mathsf{S}}$ with $\lambda_1^{\mathsf{S}} \geqslant 0$ (extensive eigendirection) and $\lambda_3^{\mathsf{S}} \leqslant 0$ (compressive eigendirection), and λ_2^{S} is either positive or negative. It can be seen from Figure 13a, that the ∇T vector aligns very well with the most contracting (negative) eigendirection of the resolved strain, *i.e.* $\boldsymbol{s}_3$, in consistency with the findings in Refs. 19 and 53. $\boldsymbol{q}^{DH}$ gives somewhat an "ideal" model[53] that accurately predicts the SGS heat flux direction in turbulent RBC (Figure 12a), similarly shown for passive scalar of isotropic turbulence[53]. *This model gives good prediction in the inertial range of LES filters, both in terms of direction and magnitude of the SGS flux vector. The time scale that adjusts the correct flux magnitude is based on the resolved strain. The model has an advantage of not requiring any additional transport equations or additional filtering, it does not have any user-adjustable constant*[53]. In an identical manner to the passive scalar, Figure 13b displays the preferential correspondence of $\boldsymbol{q}^{nl}$ direction with the direction of the most extensive eigenvector $\boldsymbol{\tau}_1^{\mathsf{GG}^t}$ of the SGS stress approached as, $\bar{\tau} \approx (\Delta^2/12)\mathsf{GG}^t$ (corresponds to the highest eigenvalue $\lambda_1^{\mathsf{GG}^t}$). This argues the essential connection between the SGS heat flux and $\bar{\tau}$ in RBC, and the very well accurate prediction of $\bar{\tau}$ using the GG^t tensor. Note that the first invariant of GG^t tensor, *i.e.* $P_{\mathsf{GG}^t} = 2(Q_\Omega - Q_{\mathsf{S}})$, identifies directly the dominant rotational focal enstrophy over the dissipation in the bulk. Moreover, its second invariant $Q_{\mathsf{GG}^t} = \mathsf{V}^2 + Q_{\mathsf{G}}^2$ also bears the L^2-norm of the vortex-stretching vector and the dominant focal tube-like structures in the bulk, in RBC. In consequence, the assumption of $\boldsymbol{q}^{DH}$ is highly sensitive to the subtle dominant topology, including the rotation by buoyant production, which becomes tightly interacted with the viscous straining. In conclusion, the tensor-diffusivity approach (derived from the tensor-viscosity) is a crucial choice in the parameterization of the SGS heat flux in turbulent RBC, and the quality of modeling the SGS stress $\bar{\tau}$ becomes the primary concern.

This manuscript was accepted by Phys. Fluids. Click here to see the version of record.

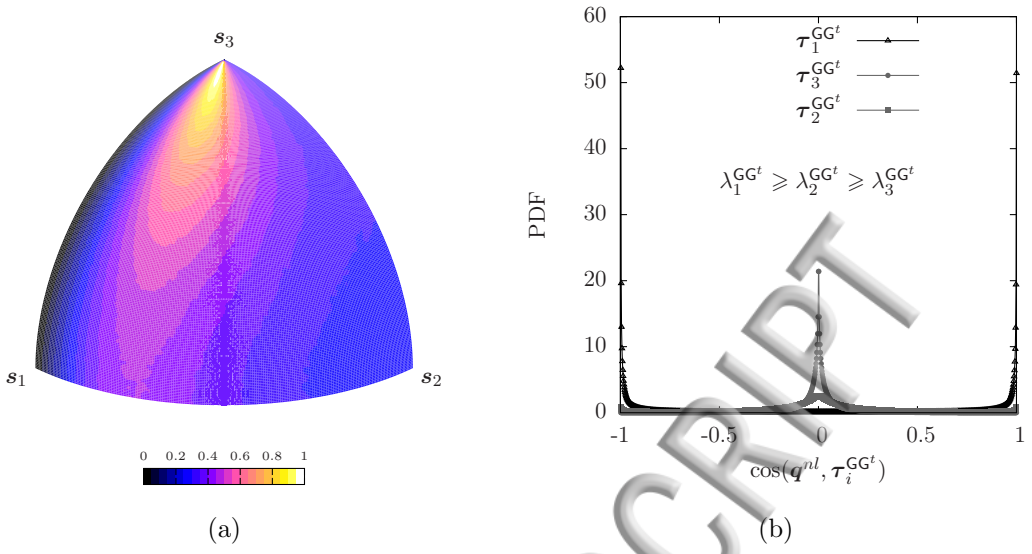

FIG. 13: (a) Alignment trends of the temperature gradient vector ,∇T, in the rate-of-strain eigenframe. (b) Displays the PDF of the cosine of the angles between the SGS heat flux approached from the nonlinear model $\boldsymbol{q}^{nl}$ and the three eigenvectors $\tau_i^{\mathsf{GG}^t}$ of the SGS stress $\bar{\tau} \approx (\Delta^2/12)\mathsf{GG}^t$.

Another candidate for the SGS heat flux parameterization can be sought in the light of the small-scale dynamics in turbulent RBC, recently studied in Dabbagh *et al.*[5]. Therein, a novel second-order tensor, $\mathsf{G}_\theta = \nabla(\boldsymbol{u}T)$ defined as the velocity-times-temperature gradient tensor, was proposed. It directly discloses the small-scale kinetic-thermal interactions and buoyant production of thermal plumes. It was also shown the relative ability of $|\mathsf{G}_\theta|$ in identifying the intensive dissipation of heat flux which deeply characterizes the action of thermal plumes. On the base of that outcome, we can consider the second-order tensor $\bar{\mathsf{G}}_\theta\bar{\mathsf{G}}_\theta^t$ (or its invariants and eigenvectors) as a possible candidate in approaching the tensorial turbulent-diffusion in RBC. Firstly, it is useful to derive the formulation of this tensor as a combination of various essential tensors, as

$$\bar{\mathsf{G}}_\theta\bar{\mathsf{G}}_\theta^t = \bar{T}^2\bar{\mathsf{G}}\bar{\mathsf{G}}^t + \bar{\mathsf{G}}\nabla\bar{T}\otimes\bar{\boldsymbol{u}}\bar{T} + \bar{\boldsymbol{u}}\bar{T}\otimes\bar{\mathsf{G}}\nabla\bar{T} + \bar{\boldsymbol{u}}\otimes\bar{\boldsymbol{u}}|\nabla\bar{T}|^2. \tag{26}$$

Upon this formulation, one can outline a set of important properties pertaining to $\bar{\mathsf{G}}_\theta\bar{\mathsf{G}}_\theta^t$, as following: [**P1**] It depends on the resolved fields that provide the condition of locality. [**P2**] Its trace contributes directly to the evolution of thermal plumes and buoyant production since $tr(\bar{\mathsf{G}}_\theta\bar{\mathsf{G}}_\theta^t) = \bar{\mathsf{G}}_\theta : \bar{\mathsf{G}}_\theta = |\bar{\mathsf{G}}_\theta|^2$, *i.e.* the L^2-norm of $\bar{\mathsf{G}}_\theta$[5]. [**P3**] It is a symmetric positive-definite second-order tensor with real positive eigenvalues and invariants. From a numerical point-of-view, this can support to some extent the desirable guarantee of stability. [**P4**]

This manuscript was accepted by Phys. Fluids. Click here to see the version of record.

It includes terms of accurate approximations (leading terms of Taylor series expansion) to the filtered-scale stress, $\bar{\mathsf{G}}\bar{\mathsf{G}}^t$, the SGS heat flux, $\bar{\mathsf{G}}\nabla\bar{T}$, and the SGS temperature variance, $|\nabla\bar{T}|^2$, embedding a combination of chief terms, which compose into the implicit algebraic formulation of the SGS heat flux[14]. This formulation is derived from the transport equation of $\bar{\boldsymbol{q}}$ by considering the production term as an actual representative term to the SGS heat flux dissipation, and thus $\bar{\boldsymbol{q}}$ is assumed to be proportionally invoked to that term. [**P5**] The components of $\bar{\mathsf{G}}_\theta\bar{\mathsf{G}}_\theta^t$ impose paramount interactions between the subgrid and supergrid (large-scale) features, such as the turbulent heat flux ,$\bar{\mathsf{G}}\nabla\bar{T}$, with the local large-scale heat transport ,$\bar{\boldsymbol{u}}\bar{T}$, that in turn are not trivial in RBC. Indeed, many studies such as Togni *et al.*[3], have displayed the inherent multi-scale mechanical energy and temperature variance budgets that occur in RBC. They gave a compound description on the inter-scale energy transfer of production/dissipation, by means of the mechanisms of buoyancy, pressure and inertial transport, between the bulk and the near-wall regions.

In order to test the validity of $\bar{\mathsf{G}}_\theta\bar{\mathsf{G}}_\theta^t$ tensor, let us investigate the alignment trends in relevant to the mixed model coordinates, just identically to the other models. To do so, we propose a possible parameterization of the SGS heat flux, given as follows

$$\bar{\boldsymbol{q}} \approx -\Delta^2|\nabla T|^{-2}|\mathsf{S}|^{-1}\mathsf{G}_\theta\mathsf{G}_\theta^t\nabla T \qquad (\equiv \boldsymbol{q}^{\mathsf{G}_\theta\mathsf{G}_\theta^t}), \tag{27}$$

and plot its properties, similarly done in Figures 12a and 13b. The new parameterization ,$\boldsymbol{q}^{\mathsf{G}_\theta\mathsf{G}_\theta^t}$, seems to roughly follow the behavior of $\boldsymbol{q}^{DH}$ (Figure 12a). As can be seen in Figure 14b, the model preferentially points towards $\boldsymbol{q}^{nl}$, identically to $\boldsymbol{q}^{DH}$; however, it additionally implicates higher diffusive orientation perpendicular to the span mixed model, just similar to the effect of the higher-order Hessian term in $\boldsymbol{q}$ (Figure 11d). This may be a result of the misalignment between ∇T and $\mathsf{G}\nabla T$ persistent in RBC, under the interactions between the large and small scales of motions. Meaning that the multiplications of the two terms, $\mathsf{G}\nabla T \otimes \boldsymbol{u}T$ and $\boldsymbol{u}T \otimes \mathsf{G}\nabla T$ (in $\mathsf{G}_\theta\mathsf{G}_\theta^t$ formulation) by ∇T, as a part of the new model, $\boldsymbol{q}^{\mathsf{G}_\theta\mathsf{G}_\theta^t}$ formulation, can play a major role in diverging the model's orientation from $\mathsf{G}\nabla T$ direction (misaligned with the thermal gradient). Therefore, the tensor $\mathsf{G}_\theta\mathsf{G}_\theta^t$ standalone may give better effectiveness using its invariants and eigenvectors. Figure 14a shows the very good alignment between $\boldsymbol{q}^{nl}$ and the highest positive (most extensive) eigenvector $\boldsymbol{\tau}_1^{\mathsf{G}_\theta\mathsf{G}_\theta^t}$. This manifests the good prediction of the buoyant production direction using a positive amplification of $|\mathsf{G}_\theta|$, *i.e.*, the highest eigenvalue $\lambda_1^{\mathsf{G}_\theta\mathsf{G}_\theta^t}$. At the end, one can suggest

This manuscript was accepted by Phys. Fluids. Click here to see the version of record.

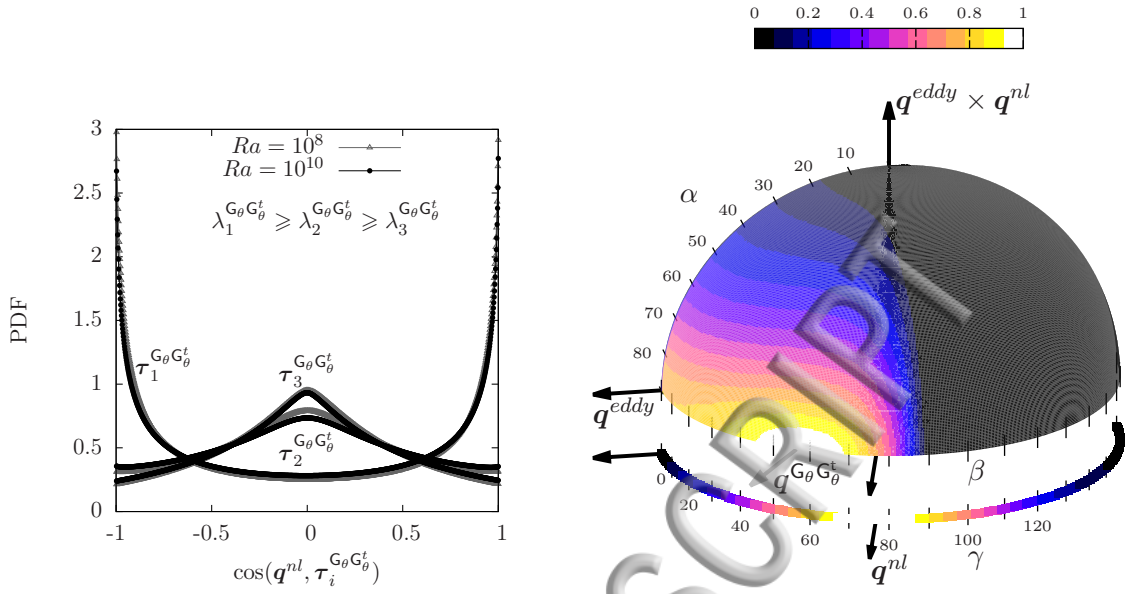

FIG. 14: (a) Displays the PDF of the cosine of the angles between the SGS heat flux approached from the nonlinear model $\boldsymbol{q}^{nl}$ and the three eigenvectors $\boldsymbol{\tau}_i^{\mathsf{G}_\theta\mathsf{G}_\theta^t}$ of $\mathsf{G}_\theta\mathsf{G}_\theta^t$ tensor, and (b) is the JPDF representation identical to Figure 12 with the parameterization $\boldsymbol{q}^{\mathsf{G}_\theta\mathsf{G}_\theta^t}$, instead.

in fairly good argument that the tensor $\bar{\mathsf{G}}_\theta\bar{\mathsf{G}}_\theta^t$, which takes into account various essential terms, including $\bar{\mathsf{G}}\bar{\mathsf{G}}^t$ (contribution to Daly and Harlow assumption), to be the key ingredient of modeling the SGS thermal turbulence in RBC. *A posteriori* assessment to such an appropriate use of $\bar{\mathsf{G}}_\theta\bar{\mathsf{G}}_\theta^t$ tensor will be an essential topic in our future research plans.

VI. CONCLUSIONS

Using our DNS database[5], *a priori* study of the underlying topological properties of the SGS features and alignment trends of existing turbulent heat flux parameterizations in LES, have been performed for turbulent Rayleigh-Bénard convection (RBC). The data corresponds to an air-filled rectangular cell of aspect ratio unity and π spanwise open-ended distance[5]. Two Rayleigh numbers have been studied, $Ra \in \{10^8, 10^{10}\}$, however due to the similarity, the low turbulent regime has been the most considered case. Generally, the main conclusions are threefold.

Firstly, a limitation in using LES eddy-viscosity models, such as WALE, QR and the

ingent S3QR[17] is found in turbulent RBC. It is based on *a posteriori* assessment and topological analysis of the models performance applying the assumption of constant turbulent Prandtl number $Pr_t = 0.4$. The ν_t-models have shown a fairly well prediction of turbulent kinetics on coarse grids. They retrieve the effect of the unfiltered scales to relax the spatial resolution in the dominant structures of vortex-stretching and viscous dissipation. Particularly, they smooth well the coarse-grained viscous dissipation associated with the energy transfer which occurs on the large negative contracting deformation in the inertial subrange. However, these models fail in capturing the subtle coupling between buoyant production and viscous straining. They restrain the production of further enstrophy pertained to the buoyancy and thermal plumes in the bulk and hence they overestimate the SGS heat flux and the overall Nu. The topological analysis, on the other hand, has corroborated the consistency of the bulk topologies in RBC with an isotropic turbulence[34].

Secondly, *a priori* investigations on the underlying physics of the SGS key ingredients *i.e.* ν_t, κ_t and Pr_t have revealed that the mean values of ν_t and κ_t are intrinsically positive in turbulent RBC at the current configurations. Upon that, it is claimed that the turbulent wind is mostly driven by the mean buoyant forces at the sidewalls (hot ascending and cold descending streams) and not by the turbulent fluctuations (Reynolds stress and negative turbulent energy production). The obtained turbulent Prandtl number, $Pr_t = \langle\nu_t\rangle/\langle\kappa_t\rangle$ has displayed a nearly constant value of 0.55 across the bulk, independently of the Ra magnitude. The highest positive values of turbulent diffusion, κ_t, are found to hold the sheet-like strain-dominated areas. They contribute to the mean expanded parts of the thermal plumes in the bulk wrapped around the vortex tubes. Instead, the highest positive values of ν_t obey the focal concentrated enstrophy in accompaniment to the strain-dominated regions. They follow in this positiveness the behavior of the small-scale dynamics and the domination of the tube-like rotation in the bulk, similarly to an isotropic turbulence. Both SGS features are found to maintain negative values corresponding to the energy backscatter ($\nu_t < 0$) and counter-gradient heat transport ($\kappa_t < 0$) in the compressed vortical structures through the bulk. Upon these observations, it has been suggested that the effective turbulent diffusion paradigm and eddy-viscosity approach (linear assumption of constant Pr_t) are only applicable in the strain-dominated areas in turbulent RBC.

Thirdly, *a priori* testing on the validity of existing SGS heat flux models has been newly performed in RBC. The study has involved the investigation of the geometric alignment trends of the most likely relative orientation imposed by the models. Firstly, it is found that the actual SGS heat flux (derived using the first two terms of the Taylor series expansion) points inside the span of the mixed model. That span is defined as the plane containing linear combination of the tensor-diffusivity vector, $\boldsymbol{q}^{nl}$ (Eq. 21), and the eddy-diffusion vector, $\boldsymbol{q}^{eddy}$ (Eq. 20). This, in turn, has certified the validity of the mixed model in RBC, similarly as in the atmospheric boundary layer[19]. The nonlinear tensor-diffusivity model, $\boldsymbol{q}^{nl}$, is very likely to be misaligned with the thermal gradient, $\boldsymbol{q}^{eddy}$. It has been argued that the rotational geometries Q_Ω are prevalent in the bulk over the strain slots, and the rate-of-rotation tensor Ω is a skew-symmetric tensor that rotates the thermal gradient vector to be always normal to $\boldsymbol{q}^{nl}$. This has eventually led to that the parameterizations linearly aligned against the spatial thermal gradient, $\boldsymbol{q}^{eddy}$, are invalid in RBC. Instead, the tensorial eddy-diffusivity approach is a crucial choice in modeling the SGS heat flux. In this framework, the most used models of Daly and Harlow[18] parameterization, $\boldsymbol{q}^{DH}$ (Eq. 24), and the straining diffusivity Peng and Davidson[14], $\boldsymbol{q}^{PD}$ (Eq. 25), parameterization, have been tested *a priori*. Both models are found to be preferentially pointed in its orientation inside the span mixed model. The thermal gradient vector tends to align fairly well with the contracting eigendirection of the rate-of-strain tensor and hence the parameterization $\boldsymbol{q}^{PD}$ is shown to be less applicable in RBC. In contrast, the $\boldsymbol{q}^{DH}$ closely approaches the direction of $\boldsymbol{q}^{nl}$ in the mixed model coordinates and the SGS heat flux is found to coincide preferentially the direction of the most extensive eigenvector of $\mathsf{G}\mathsf{G}^t$ tensor.

Finally, a new approach of using $\bar{\mathsf{G}}_\theta \bar{\mathsf{G}}_\theta^t$ tensor in modeling the SGS thermal turbulence in RBC, has been suggested. It contains a combination of chief components, including the $\bar{\mathsf{G}}\bar{\mathsf{G}}^t$ tensor, owning properties similar to the implicit algebraic formulation of the SGS heat flux. Following *a priori* examination of one candidate $\bar{\boldsymbol{q}} \approx -\Delta^2 |\nabla T|^{-2} |\mathsf{S}|^{-1} \mathsf{G}_\theta \mathsf{G}_\theta^t \nabla T$, it is found that the new model performs almost similar to $\boldsymbol{q}^{DH}$, that in turn encourages its application. *A posteriori* throughout investigations on the appropriate use of $\bar{\mathsf{G}}_\theta \bar{\mathsf{G}}_\theta^t$ tensor in modeling the SGS heat flux in RBC, will be our primary concern in the future.

ACKNOWLEDGMENTS

This work has been financially supported by the *Ministerio de Economía y Competitividad*, Spain (ENE2014-60577-R), a Ramón y Cajal postdoctoral contract (RYC-2012-11996), a Ph.D scholarship by the *Tishreen University*, Syria, and the Russian Science Foundation (project 15-11-30039). Calculations have been performed on the IBM MareNostrum supercomputer at the Barcelona Supercomputing Center and on the HPC4 supercomputer at the Kurchatov Institute in Moscow. The authors thankfully acknowledge these institutions.

REFERENCES

[1]E. D. Sigga. High Rayleigh number convection. *Annual Reviews of Fluid Mechanics*, **26**:137, 1994.

[2]K. Hanjalić. One-point closure models for buoyancy-driven turbulent flows. *Annual Reviews of Fluid Mechanics*, **34**:321–347, 2002.

[3]R. Togni, A. Cimarelli, and E. D Angelis. Physical and scale-by-scale analysis of Rayleigh-Bénard convection. *Journal of Fluid Mechanics*, **782**:380–404, 2015.

[4]F. Chillà and J. Schumacher. New perspectives in turbulent Rayleigh-Bénard convection. *The European Physics Journal E*, **35**:58, 2012.

[5]F. Dabbagh, F. X. Trias, A. Gorobets, and A. Oliva. On the evolution of flow topology in turbulent Rayleigh-Bénard convection. *Physics of Fluids*, **28**:115105, 2016.

[6]R. J. A. M. Stevens, D. Lohse, and R. Verzicco. Prandtl and Rayleigh number dependence of heat transport in high Rayleigh number thermal convection. *Journal of Fluid Mechanics*, **688**:31, 2011.

[7]E. P. van der Poel, R. Verzicco, S. Grossmann, and D. Lohse. Plume emission statistics in turbulent Rayleigh- Bénard convection. *Journal of Fluid Mechanics*, **772**:5–15, 2015.

[8]T. M. Eidson. Numerical simulation of the turbulent Rayleigh-Bénard problem using subgrid modelling. *Journal of Fluid Mechanics*, **158**:245–268, 1985.

[9]S. Peng and L. Davidson. Comparison of subgrid-scale models in LES for turbulent convection flow with heat transfer. pp 5.24–5.35, Manchester, U.K., 1998.

[10]M. Germano, U. Piomelli, P. Moin, and W. H. Cabot. A dynamic subgrid-scale eddy viscosity model. *Physics of Fluids A*, **3**:1760–1765, 1991.

[11]D. K. Lilly. A proposed modification of the Germano subgrid-scale closure method. *Physics of Fluids A*, **4**:633–635, 1992.

[12]S. H. Peng, K. Hanjalic, and L. Davidson. Large-eddy simulation and deduced scaling analysis of Rayleigh-Bénard convection up to $Ra = 10^9$. *Journal of Turbulence*, **7**:66, 2006.

[13]T. Czarnota, T. Wetzel, and C. Wagner. *Large Eddy Simulation of Turbulent Thermal Convection Using Different Subgrid-Scale Models*, pp 505–514. Springer International Publishing, Cham, 2016.

[14]S. Peng and L. Davidson. On a subgrid-scale heat flux model for large eddy simulation of turbulent thermal flow. *International Journal of Heat and Mass Transfer*, **45**:1393–1405, 2002.

[15]N. Foroozani, J. J. Niemela, V. Armenio, and K. R. Sreenivasan. Influence of container shape on scaling of turbulent fluctuations in convection. *Physical Review E*, **90**:063003, 2014.

[16]C. Meneveau, T. S. Lund, and W. H. Cabot. Lagrangian dynamic subgrid-scale model of turbulence. *Journal of Fluid Mechanics*, **319**:353–385, 1996.

[17]F. X. Trias, D. Folch, A. Gorobets, and A. Oliva. Building proper invariants for eddy-viscosity subgrid-scale models. *Physics of Fluids*, **27**:065103, 2015.

[18]B. J. Daly and F. H. Harlow. Transport equations in turbulence. *Physics of Fluids*, **13**:2634, 1970.

[19]C. W. Higgins, M. B. Parlange, and C. Meneveau. The heat flux and the temperature gradient in the lower atmosphere. *Geophysical Research Letter*, **31**:L22105, 2004.

[20]F. Dabbagh, F. X. Trias, A. Gorobets and A. Oliva. Spectrally-consistent regularization of turbulent Rayleigh-Bénard convection. *6th European Conference on Computational Fluid Dynamics*(International Center for Numerical Methods in Engineering, 2014), pp. 7144–7155.

[21]A. Oberbeck. Ueber die Wärmeleitung der Flüssigkeiten bei Berücksichtigung der Strömungen infolge von Temperaturdifferenzen. *Annalen der Physik*, **243**:271–292, 1879.

[22]J. V. Boussinesq. Théorie analytique de la chaleur. *(Gauthier-Villars Paris)*, **2**, 1903.

[23]R. W. C. P. Verstappen and A. E. P. Veldman. Symmetry-preserving discretization of turbulent flow. *Journal of Computational Physics*, **187**:343–368, 2003.

[24]F. X. Trias and O. Lehmkuhl. A self-adaptive strategy for the time-integration of Navier-

Stokes equations. *Numerical Heat Transfer, part B*, **60**(2):116–134, 2011.

[25]A. J. Chorin. Numerical solution of the Navier-Stokes equation. *Mathematics of Computation*, **22**:745–762, 1968.

[26]F. X. Trias, M. Soria, C. D. Pérez-Segarra, and A. Oliva. Direct numerical simulation of two- and three-dimensional turbulent natural convection flows in a differentially heated cavity of aspect ratio 4. *Journal of Fluid Mechanics*, **586**:259–293, 2007.

[27]R. A. J. M. Stevens and R. Verzicco and D. Lohse. Radial boundary layer structure and Nusselt number in Rayleigh-Bénard convection. *Journal of Fluid Mechanics*, **643**:495–507, 2010.

[28]G. Grötzbach. Spatial resolution requirements for direct numerical simulation of the Rayleigh-Bénard convection. *Journal of Computational Physics*, **49**:241–264, 1983.

[29]O. Shishkina, R. J. A. M. Stevens, S. Grossmann, and D. Lohse. Boundary layer structure in structure in turbulent thermal convection and consequences for the required numerical resolution. *New Journal of Physics*, **12**:075022, 2010.

[30]F.Nicoud and F. Ducros. Subgrid-scale stress modelling based on the square of the velocity gradient tensor. *Flow, Turbulence and Combustion*, **62**:183–200, 1999.

[31]R. Verstappen. When does eddy viscosity damp subfilter scales sufficiently? *Journal of Scientific Computing*, **49**:94–110, 2011.

[32]M. S. Chong, A. E. Perry, and B. J. Cantwell. A general classification of three-dimensional flow fields. *Physics of Fluids A*, **2**:765, 1990.

[33]H. M. Blackburn, N. N. Mansour, and B. J. Cantwell. Topology of fine-scale motions in turbulent channel flow. *Journal of Fluid Mechanics*, **310**:269–292, 1996.

[34]A. Ooi, J. Martin, J. Soria, and M. S. Chong. A study of the evolution and characteristics of the invariants of the velocity-gradient tensor in isotropic turbulence. *Journal of Fluid Mechanics*, **381**:141, 1999.

[35]C. B. da Silva and J. C. F. Pereira. Invariants of the velocity-gradient, rate-of-strain, and rate-of-rotation tensors across the turbulent/nonturbulent interface in jets. *Physics of Fluids*, **20**(5):055101, 2008.

[36]F. X. Trias, O. Lehmkuhl, A. Oliva, C. D. Pérez-Segarra and R. W.C. P. Verstappen . Symmetry-preserving discretisation of Navier-Stokes equations on collocated unstructured grids. *Journal of Computational Physics*, **258**(1):246–267, 2014.

[37]F. X. Trias, A. Gorobets and A. Oliva. A simple approach to discretize the viscous term

with spatially varying (eddy-)viscosity. *Journal of Computational Physics*, **253**(1):405–417, 2013.

[38]M. Chertkov, A. Pumir, and B. I. Shraiman. Lagrangian tetrad dynamics and the phenomenology of turbulence. *Physics of Fluids*, **11**(8):2394–2410, 1999.

[39]J. Jiménez, A. A. Wray, P. G. Saffman, and R. S. Rogallo. The structure of intense vorticity in isotropic turbulence. *Journal of Fluid Mechanics*, **255**:65–90, 1993.

[40]S. W. Churchill. A Reinterpretation of the Turbulent Prandtl Number. *Industrial & Engineering Chemistry Research*, **41**:6393–6401, 2002.

[41]J. Kim and P. Moin. Transport of passive scalars in a turbulent channel flow. *In Turbulent Shear Flows 6*. pp 85–96, Toulouse, France, 1987. Berlin: Springer.

[42]J. Pallares and L. Davidson. Large-eddy simulations of turbulent heat transfer in stationary and rotating square ducts. *Physics of Fluids*, **14**:2804, 2002.

[43]P. Sagaut. *Large Eddy Simulation for Incompressible Flows: An Introduction*. Third edition. Springer, 2006.

[44]P. Moin, K. Squires, W. Cabot, and S. Lee. A dynamic subgridscale model for compressible turbulence and scalar transport. *Physics of Fluids A: Fluid Dynamics*, **3**:2746–2757, 1991.

[45]I. Otic. One equation subgrid model for liquid metal forced convection. *The 8th International Topical Meeting on Nuclear Reactor Thermal Hydraulics, Operation and Safety (NUTHOS-8)*. Shanghai, China, October 2010.

[46]A. Leonard. Large-eddy simulation of chaotic convection and beyond. *35th Aerospace Sciences Meeting and Exhibit, AIAA paper*. volume 1997, Reno, NV, U.S.A.

[47]G. L. Eyink. Multi-scale gradient expansion of the turbulent stress tensor. *Journal of Fluid Mechanics*, **549**:159, 2006.

[48]G. S. Winckelmans, A. A. Wary, O. V. Vasilyev and H. Jeanmart. Explicit-filtering large-eddy simulation using the tensor-diffusivity model supplemented by a dynamic Smagorinsky term. *Physics of Fluids*, **13**:1385, 2001.

[49]S. J. Kimmel and J. A. Domaradzki. Large eddy simulations of Rayleigh-Bénard convection using subgrid scale estimation model. *Physics of Fluids*, **12**:169–184, 2000.

[50]U. Burr, W. Kinzelbach, and A. Tsinober. Is the turbulent wind in convective flows driven by fluctuations? *Physics of Fluids*, **15**:2313, 2003.

[51]Y. Huang and Q. Zhou. Counter-gradient heat transport in two-dimensional turbulent Rayleigh-Bénard convection. *Journal of Fluid Mechanics*, **737**, 2013.

[52]R. Krishnamurti and L. N. Howard. Large-Scale Flow Generation in Turbulent Convection. *Proceedings of the National Academy of Sciences of the United States of America*. **78**, pp 1981–1985. National Academy of Sciences, 1981.

[53]S. G. Chumakov. A *priori* study of subgrid-scale flux of a passive scalar in isotropic homogeneous turbulence *Physical Review E* , **78**:036313, 2008.

[54]A. Liberzon, B. Lüthi, M. Guala, W. Kinzelbach, and A. Tsinober. *On Anisotropy of Turbulent Flows in Regions of "Negative Eddy Viscosity"*, pp 85–88. Springer Berlin Heidelberg, Berlin, Heidelberg, 2007.

[55]K. Horiuti. Coherent Structure and Subgrid-Scale Energy Transfer in Turbulence. In *IUTAM Symposium on Geometry and Statistics of Turbulence*, pp 249–254. Springer, 2001.

[56]D. Carati, G. S. Winckelmans, and H. Jeanmart. On the modelling of the subgrid-scale and filtered-scale stress tensors in large-eddy simulation. *Journal of Fluid Mechanics*, **441**:119–138, 2001.

[57]J. Smagorinsky. General circulation experiments with primitive equations. *Monthly Weather Review*, **91**:99–164, 1963.